ABSTRACT

Title of thesis: MEASUREMENT AND SCALING ANALYSIS OF ROTOR-INDUCED SEDIMENT MOBILIZATION

Gino Perrotta, Master of Science, 2014

Thesis directed by: Professor Anya Jones
Department of Aerospace Engineering

Flow visualization and particle imaging velocimetry (PIV) experiments were conducted in a water tank to investigate the effects of rotor wake and sediment properties on rotor-induced sediment mobilization during hover in ground effect. The two-phase flow was separated into the carrier phase and the dispersed phase for characterization. The carrier phase was studied using PIV to acquire time-resolved planar velocity measurements for a field of view within the rotor wake. The rotor-induced flow was confirmed to be dominated by blade tip vortices and was characterized primarily in terms of the vortex characteristics. Vortices were identified using a tracking function, and were compared to the Lamb–Oseen vortex velocity profile to evaluate their size and strength. The rotor-induced flow was also characterized in terms of wall-jet velocity and turbulent kinetic energy. The dispersed phase was separated using image filtering procedures and was quantified by identifying mobilized sediment particles visible in the field of view. Characteristics

of the rotor-induced flow and quantification of sediment mobilization were each averaged over time for several rotor rotations to reduce the effects of wake aperiodicity and asymmetry. New parameter groups were created by combining rotor-induced sediment mobilization system characteristics and each was inspected for correlation with sediment mobilization. Three parameter groups which correlated for all cases measure here are identified and discussed.

Measurement and Scaling Analysis of Rotor-Induced Sediment Mobilization

by

Gino Perrotta

Thesis submitted to the Faculty of the Graduate School of the
University of Maryland, College Park in partial fulfillment
of the requirements for the degree of
Master of Science
2014

Advisory Committee:
Professor Anya Jones, Chair/Advisor
Professor J. Gordon Leishman
Professor Kenneth Kiger

Acknowledgments

I would like to thank my advisor, Dr. Anya Jones, for guidance and patience throughout this endeavor. I am sincerely grateful for her academic mentorship, which has contributed a great deal to my education and to this thesis.

Thanks also to my thesis review committee, Dr. Leishman and Dr. Kiger, who have each contributed to my education in the classroom and laboratory.

I would also like to thank my fellow students of the Low Reynolds Number Aerodynamics Laboratory for their assistance and encouragement.

Finally, thanks to the Air Force Office of Scientific Research for their the financial support of this thesis through Douglas Smith and the Multidisciplinary University Research Initiative Grant No. W911NF0410176.

Table of Contents

List of Tables

List of Figures

Nomenclature

c	m	Rotor blade chord
d	m	Deposition depth
e	–	Particle coefficient of restitution
g	$\mathrm{kg\,m\,s^{-2}}$	Gravitational acceleration
k	$\mathrm{m^2\,s^{-2}}$	Turbulent kinetic energy, $= \frac{1}{N}\sum_{i=1}^{N}\frac{1}{2}((u_i-\bar{u})^2+(v_i-\bar{v})^2)$
r	m	Radial distance from vortex center
$\bar{r}$	–	Normalized radial distance from vortex center, $= \frac{r}{R_c}$
$\bar{r}^*$	–	Laminar-turbulent transition radius
t^{-1}	Hz	Blade tip passage frequency
x, y, z	m	Cartesian coordinate system
u, v, w	$\mathrm{m\,s^{-1}}$	Velocities in x, y, and z
A_{vortex}	$\mathrm{m^2}$	Vortex core area, $= \pi R_c^2$
D_p	m	Particle diameter
H	m	Reference vertical dimension
L_i	m	Topographic horizontal dimensions
L_R	m	Reference horizontal dimension
L^*	m	Monin–Obhukov atmospheric stability length
R	m	Rotor radius
R^2	–	Goodness-of-fit statistic
R_c	m	Vortex core radius
R_{e_v}	–	Vortex Reynolds number, $= \frac{\rho V_{\theta\,\max} R_c}{\mu} = \frac{\Gamma}{\nu}$
R_{i_v}	–	Vortex Richardson number, $= \frac{\frac{2V_\theta}{r^2}\frac{\partial}{\partial r}(V_\theta\, r)}{\left(r\frac{\partial}{\partial r}\frac{V_\theta}{r}\right)^2}$
R_L	–	Relaminarization parameter, $= \frac{R_{i_v}}{R_{e_v}^{1/4}}$
U_F	$\mathrm{m\,s^{-1}}$	Terminal velocity
U	m	Horizontal wind speed
U_{char}	$\mathrm{m\,s^{-1}}$	Characteristic velocity
U_{wall}	$\mathrm{m\,s^{-1}}$	Wall-jet velocity
U_*	$\mathrm{m\,s^{-1}}$	Friction velocity
U_{*t}	$\mathrm{m\,s^{-1}}$	Threshold friction velocity
V_{tip}	$\mathrm{m\,s^{-1}}$	Rotor tip velocity
V_θ	$\mathrm{m\,s^{-1}}$	Vortex tangential velocity
$V_{\theta\,\max}$	$\mathrm{m\,s^{-1}}$	Vortex peak swirl velocity
z_0	m	Surface roughness height

α	–	Oseen constant = 1.25643
η	m	Topographic vertical dimensions
μ	$\mathrm{kg\,m^{-1}\,s^{-1}}$	Fluid dynamic viscosity
ν	$\mathrm{m^2\,s^{-1}}$	Fluid kinematic viscosity
ρ	$\mathrm{kg\,m^{-3}}$	Fluid density
ρ_p	$\mathrm{kg\,m^{-3}}$	Particle density
Γ_v	$\mathrm{m^2\,s^{-1}}$	Vortex circulation

CMOS	Complementary Metal Oxide Semiconductor (camera)
Nd:YLF	Neodymium-doped Yttrium-Lithium-Flouride (laser)
PIV	Particle Imaging Velocimetry
rpm	Revolutions per minute

Chapter 1: Introduction

1.1 Helicopter Brownout

Because of their ability to hover, helicopters hold a distinct advantage over fixed-wing vehicles in many specific missions. Search and rescue, rapid deployment, rapid retrieval, and many other missions require the ability to hover and so can only be completed by a helicopter. However, helicopters hovering near to the ground can experience a set of complex and dangerous conditions. The combination of hover and ground effect is one of the very few cases in which the vehicle's wake remains near to the vehicle. Vehicles in motion (which flying fixed wing aircraft must always be) produce a wake which trails behind them and so does not affect the vehicle's own flight environment. A helicopter hovering far from the ground produces a wake that convects downward away from the vehicle. However, a helicopter hovering near the ground does not move away from the wake, nor is the wake able to move far from the vehicle.

This work examines the flow caused by hover in ground effect over a loose sediment bed. This set of circumstances can lead to a dangerous phenomenon called "helicopter brownout" in which the vehicle is engulfed by a sediment cloud created by its own rotor wake. An example of brownout can be seen in Fig. 1.1. The

Figure 1.1: Rotor-induced sediment mobilization, or "brownout" (Courtesy of Optical Air Data Systems LLC.)

brownout cloud can develop quickly, leaving the pilot unable to fly based on visual cues. Brownout can also create visual illusions of false motion or incorrect horizon. These hazards have led to a large number of crashes, especially in areas with loose, fine sediment that mobilizes easily [1]. There are also several less immediate hazards of brownout. Suspended sediment can impact the leading edge of the rapidly moving rotor blades, severely abrading the surface [2]. Airborne sediment can also abrade the engine components.

1.2 Objectives

To reduce the hazards caused by brownout, it is necessary to better understand the relationship between wake characteristics and sediment mobilization. The mechanics of sediment uplift by rotor wake have only recently begun to be understood.

Figure 1.2: Toroidal sediment cloud (Courtesy of AWI)

To progress further, studies must be performed to better understand the system's sensitivity to rotor and environmental parameters. Experience has indicated that the system is very complex and difficult to characterize. For example, different helicopters experience different intensities and shapes of sediment clouds [3]. In some cases, as shown in Fig. 1.2, the sediment cloud is toroidal. In these cases, an area of the ground remains visible and abrasion by sediment is diminished due the the distance between the helicopter and the cloud. In other cases, as shown previously in Fig. 1.1, the dust cloud fills in entirely.

Because operating a helicopter in brownout is dangerous., it is more practical for the majority of rotor-induced sediment mobilization studies to be conducted using models. The drawback of small-scale experiments is that it is difficult to properly scale a model of rotor-induced sediment mobilization. While experimental scaling of

aerodynamics is fairly well understood, scaling of multi-phase systems is not simple. Without a measure of the scaling physics for the brownout system, it is difficult to translate measurements in small-scale experiments to a better understanding of full-scale applications.

This thesis aims to contribute by measuring sediment mobilization under a variety of conditions and inspecting the dependency of sediment mobilization on system parameters. The primary goal of this work is to identify a parameter group which can be used to predict and relate brownout intensity over a range of conditions. Such a parameter would aid in understanding rotor-induced sediment mobilization behavior and could allow the comparison of results for systems at different scales.

1.3 Literature Review

Rotor-induced sediment mobilization and its alleviation were first researched roughly half of a century ago. White and Vidal studied the rotor wake shape in ground effect and the resulting sediment mobilization [4]. Kuhn looked for threshold conditions that defined the lower limits of rotor-induced sediment mobilization [5]. However, most of the research on the topic has been conducted in the past decade [6, 7]. Additional relevant research has been conducted on the constituent fields of rotor-induced sediment mobilization, including helicopter wake aerodynamics, sediment transport, and experimental scaling [8, 9]. The more recent research is discussed below.

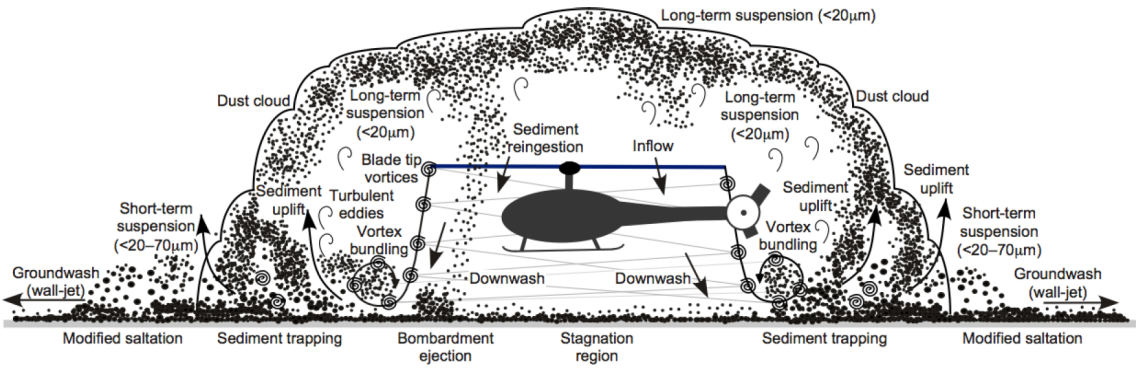

Figure 1.3: Flow features identified in observation of brownout [13]

1.3.1 Rotor Wake

The studies of wake aerodynamics that are particularly relevant here are those that focus on a rotor wake in ground effect. Because the sediment that forms a brownout cloud is originally on the ground, brownout occurs when the helicopter is close to the surface. Most studies of a rotor wake in ground effect have focused on the effects of the ground's proximity on rotor performance [10–12]. In general, these studies show that ground effect increases the thrust provided by the rotor.

Other studies, such as one by Lee et al. and another by Light and Norman, have observed the wake in detail to identify the mechanics and structures of the flow [14, 15]. A diagram of these structures is shown in Fig. 1.3. The primary conclusion of these works is that the dominant feature of a rotor wake in ground effect is the set of helical vortices that trail from the tip of each rotor blade. Because the tip vortices are periodic, they are not visible in a time-averaged view of the rotor wake. Glucksman-Glaser showed that for studies of rotor-induced sediment mobilization, velocity measurements which inherently average over a long time are

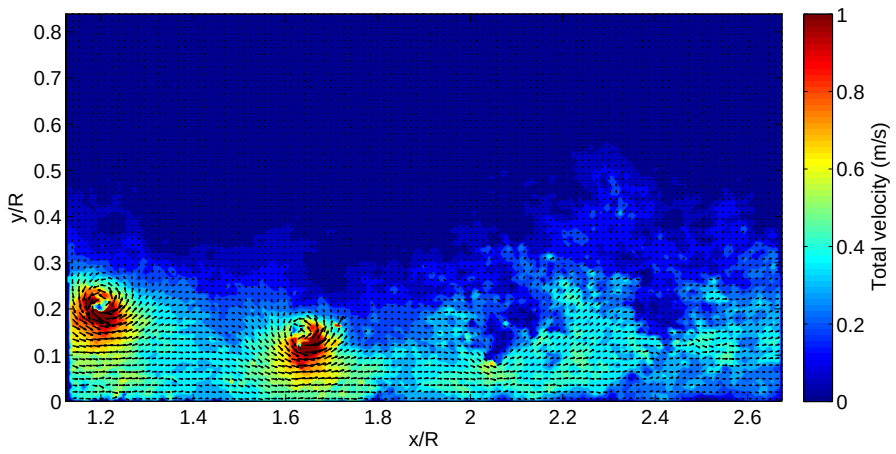

Figure 1.4: Instantaneous velocity field of a rotor wake in ground effect

insufficient [16]. Figure 1.4 shows an instantaneous velocity field in a rotor wake in ground effect, and Fig. 1.5 shows the same velocity field averaged over time. The tip vortices are only clearly present in the instantaneous velocity field.

When a rotor wake encounters a ground plane, it expands, while a wake out of ground effect contracts. Wake expansion carries the vortices with the wake and leads to vortex core stretching. Core stretching prolongs and intensifies the vortices as they convect, giving them a greater influence on the wake in ground effect than would otherwise be the case [17]. Following from this, Sydney et al. have shown that these tip vortices are the primary source of sediment mobilization during brownout [13]. It has also been noted by Johnson et al. that irregular wake structures such as tip vortex bundles contribute significantly to sediment uplift [7].

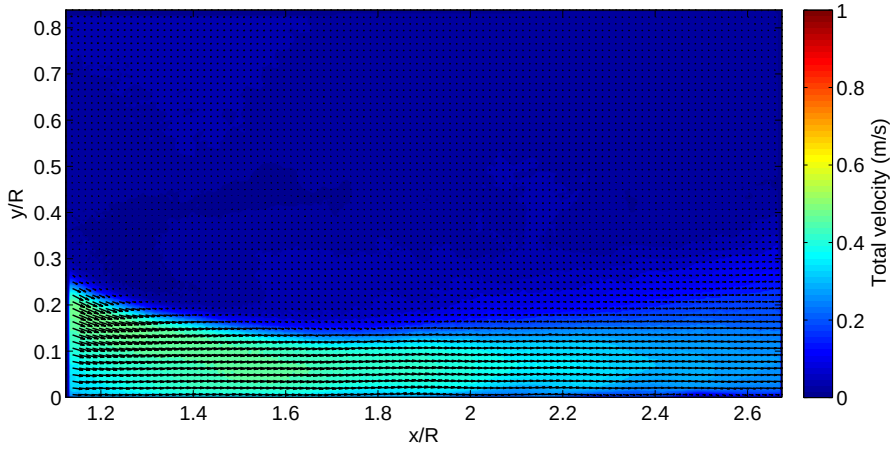

Figure 1.5: Time-averaged velocity field of a rotor wake in ground effect

1.3.2 Sediment Transport

Aeolian science deals with erosion by wind, and fluvial science with erosion by flowing water. Both of these fields study the conditions required for sediment to lift and move. Studies in these fields have identified three primary forms of sediment motion: creep, saltation, and bombardment. These motions are illustrated in Fig. 1.6. A thorough discussion of sediment transport physics is documented by Greeley and Iverson [18].

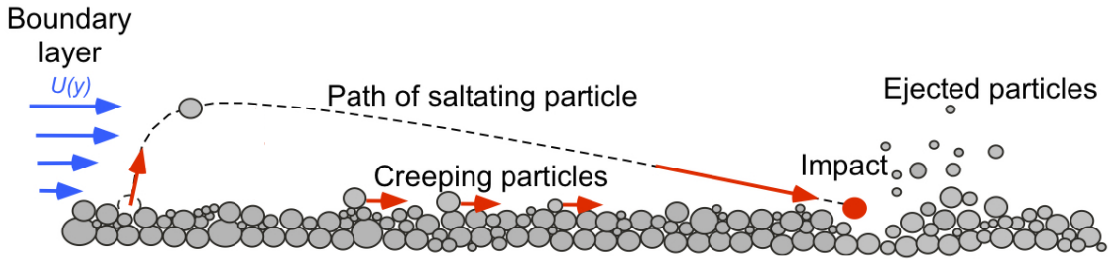

Figure 1.6: Modes of sediment mobilization [19]

The first mode of motion, called creep, describes particles that roll or slide across the surface without lifting off of the ground. A creeping particle that gains enough energy can bounce off of the surface and travel a short distance above the ground. This mode of sediment transport is called saltation. The final mode of motion, bombardment, describes the event surrounding a saltating particle as it returns to the ground, impacting other particles and transferring energy to them. The impacted particles will begin to creep or saltate as a result of this bombardment, which continues the cycle. An additional mode, suspension, describes particles which do not return to the sediment bed. Which mode of motion occurs is determined by the terminal velocity of the particle and the local friction velocity. The terminal velocity, U_F, is related to the particle's weight (and thus to its size and density), and the drag from the flow. The friction velocity, U_*, is a measure of the stress exerted on the particle by the fluid moving past it. In cases for which ${}^{U_F}/_{U_*} > 1$, the particle motion is saltation, and the particle will return to the sediment bed. For ${}^{U_F}/_{U_*} < 1$, the particle is suspended in the fluid, and will be carried along with it [18].

An important consideration in studies of sediment transport is the threshold conditions at which sediment motion begins. One commonly used quantity is the threshold friction velocity, which is the minimum U_* at the sediment bed surface which is required to dislodge and move sediment particles. The threshold friction velocity, U_{*t}, is related to both the characteristics of the individual sediment particles and to those of the sediment bed, such as particle density and cohesion [20]. The sediment's terminal velocity is also a useful parameter in assessing mobilization, as its ratio with the local friction velocity determines the mode of sediment motion.

It is therefore these two parameters, U_{*_t} and U_F, which will be used in addition to particle diameter and density to describe the sediment properties in this study of rotor-induced sediment mobilization.

1.3.3 Scaling

Previous studies of brownout have been conducted at a variety of scales. In a few cases, such as the Sandblaster project from DARPA, brownout was studied for a full scale helicopter [21]. These experiments are exceptionally difficult and expensive, and so the majority of studies are conducted on small scale recreations of the rotor-induced sediment mobilization system [7, 13, 19, 22]. An important discussion in these cases is the effect of dynamic scaling on an experimental model. The results of these investigations are only useful if the relationship to a full-scale system can be determined. This relationship is established through the use of of similarity parameters.

In aerodynamics, flow similarity is accomplished by matching the Reynolds number, the Mach number, and the relative geometry of the experiment to those of the full scale system. For low speed aerodynamics experiments, the Reynolds number is made as close as is feasible, and the Mach number is assumed to be sufficiently low. This is regarded as acceptable due to the minimal sensitivity of fluids to Mach number in the low subsonic range, and the relative difficulty of altering

the local speed of sound. This complication arises from the inherent coupling of the Reynolds number and Mach number. Similar coupling is a source of significant complexity in the scaling analysis of rotor-induced sediment mobilization.

For sediment physics, Greeley and Iverson proposed 15 similarity parameters based on dimensional analysis of 18 variables that define the system of wind blown sediment [18]. All 15 of these are shown in Tab. 1.1, however experimentally matching the entire set of parameters would be prohibitively difficult. Recently, a study by Baharani suggested that a smaller selection of parameters could be used in the characterization of brownout [22]. The exclusion of the other parameters is similar to neglecting the Mach number; in the particular conditions studied here, the system sensitivity to the excluded parameters is assumed to be minimal compared to the included ones. The five parameters identified as most important to sediment uplift in brownout are:

$\frac{\rho_p}{\rho}$	Particle to fluid density ratio
$\frac{U_{\text{char}}}{U_{*_t}}$	Characteristic velocity to threshold velocity ratio
$\frac{D_p}{R}$	Particle diameter to rotor radius ratio
$\frac{U_{\text{char}}}{\sqrt{(\frac{\rho_p}{\rho}-1)gD_p}}$	Densimetric Froude number
$\frac{U_{\text{char}}}{U_F}$	Characteristic velocity to terminal velocity ratio

Table 1.1: Similarity parameters for aeolian phenomena [18]

Parameter	Symbol
Deposition depth	d/L_r
Particle diameter to characteristic length ratio	D_p/L_r
Froude number	U^2/gL_r
Coefficient of restitution	e
Ratio of wind speed to particle terminal speed	U/U_F
Topographical geometric similarity (a)	L_i/L_r
Topographical geometric similarity (b)	H/L_r
Topographical geometric similarity (c)	η/L_r
Roughness similarity	z_o/L_r
Boundary layer stability similarity	L^*/L_r
Reynolds number	UL_r/ν
Friction speed ratio (a)	U/U_{*t}
Friction speed ratio (b)	U/U_*
Density ratio	ρ/ρ_p
Time scale	U_t/L_r

The ratio of particle density and fluid density impacts both the local friction velocity and the terminal velocity of the particles. The Froude number and the ratios of characteristic velocity to U_{*t} and U_F dictate the mode of sediment motion. The ratio of particle diameter to rotor radius enforces geometric similarity.

Even after reducing the number of scaling parameters to five, it is not feasible to exactly match a small-scale model to the full-scale system. The primary difficulty in doing so is the inherent coupling between these scaled characteristics. For example, a small scale model rotor will have to be operated over proportionally small sediment particles. These small particles would have a much lower terminal velocity, unless the density of either the particles or the fluid is changed. However,

the ratio of these two densities must also be maintained for all of the similarity parameters to be matched. Because of these couplings, any experimental design will result in mismatched values for several of these scaling parameters. Because these parameters cannot all be properly matched, it is important to study the effects that their variations have on rotor-induced sediment mobilization.

As a precursor to this work, Buckingham-Pi dimensional analysis was applied to the rotor-induced sediment mobilization system by Glucksman-Glaser [19]. This effort was in order to study variations in sediment mobilization resulting from variations in scaling parameters and to identify dimensionless parameter groups which correlate with rotor-induced sediment mobilization severity. This dimensional analysis was based on the parameters in Tab. 1.2 and suggested four new dimensionless groups as likely scaling parameters for rotor-induced sediment mobilization.

The proposed scaling parameters were [19]:

$\frac{\Gamma_v}{D_p U_{*_t}}$	called the stationary inertia ratio
$\frac{\Gamma_v}{D_p U_F}$	called the mobile inertia ratio
$\frac{V_{\theta\,\max}}{U_F}$	called the terminal-swirl velocity ratio
$\frac{V_{\theta\,\max}}{U_{*_t}}$	called the threshold-swirl velocity ratio
$\frac{V^2_{\theta\,\max}}{U_F U_{*_t}}$	called the terminal/threshold-swirl velocity ratio

Table 1.2: Dependent variables used for Buckingham-Π analysis [19]

Parameter	Symbol	Units	Basic units
Rotor radius	R	m	L
Blade chord	c	m	L
Particle diameter	D_p	m	L
Characteristic flow velocity	U_{char}	ms^{-1}	LT^{-1}
Gravitational constant	g	ms^{-2}	LT^{-2}
Particle terminal velocity	U_F	ms^{-1}	LT^{-1}
Boundary layer thickness	L^*	m	L
Kinematic viscosity	ν	m^2s	L^2T
Threshold friction velocity	U_{*t}	ms^{-1}	LT^{-1}
Sediment density	ρ_p	kg m^{-3}	ML^{-3}
Fluid density	ρ	kg m^{-3}	ML^{-3}
Blade passage frequency	t^{-1}	s^{-1}	T^{-1}
Vortex circulation	Γ_v	m^2s	L^2T^{-1}
Vortex core size	R_c	m	L
Peak swirl velocity	$V_{\theta\,\text{max}}$	ms^{-1}	LT^{-1}
Vortex area	A_{vortex}	m^2	L^2
Rotor tip speed	V_{tip}	ms^{-1}	LT^{-1}

Each of these proposed parameters in some way relates to the velocity ratios suggested by Baharani. In Glucksman-Glaser's parameters, the characteristic velocity is replaced by tip vortex characteristics. This modification is qualitatively supported by the previously identified dominance of the tip vortices in rotor-induced sediment mobilization. However, there was not sufficient data in Glucksman-Glaser's study to properly evaluate the proposed similarity parameters. Part of the current study will be to apply new data to the analysis of these results.

1.4 Thesis Overview

This thesis describes the process and results of two years of research in the University of Maryland Low Reynolds Number Aerodynamics Laboratory (LRAL). This research is a parametric study of a small-scale model of rotor-induced sediment mobilization using optical measurement techniques and novel data processing. The goal of this thesis is to quantitatively analyze the dependencies between dominant rotor wake features identified by previous studies and sediment mobilization.

Chapter 2 presents the hardware and software used in this experiment. The primary focus of this section is the data processing procedure which was developed for this work. Chapter 3 presents the results of the measurements described in chapter 2. Chapter 3 then describes the process used to identify and assess system dependencies. Three correlated parameter groups are proposed and analyzed, and a physical interpretation of each parameter is given. In chapter 4, the conclusions of this thesis are summarized. The strengths and limitations of the procedure applied in this thesis are discussed, and suggestions for adaptation and extension of this work are provided.

1.5 Summary

This chapter has introduced the phenomenon of brownout and has reviewed previous material to aid in understanding the complex, multi-phase flow of rotor-induced sediment mobilization. Relevant concepts of rotor wake and sediment trans-

port physics have been introduced. It was noted that rotor-induced sediment mobilization is connected to the rotor blade tip vortices, but also that the dependencies are complex and have not yet been characterized. Additionally, studies of the scaling physics associated with rotor-induced flow and sediment transport were presented. Previous works have shown that small-scale rotor-induced sediment mobilization struggles to simultaneously address scaling for both rotor aerodynamics and sediment transport. Recently proposed scaling parameters for rotor-induced sediment mobilization were discussed.

Chapter 2: Description of Experiment

The observation and measurement of small-scale rotor-induced sediment mobilization was performed here using planar optical techniques for a rotor and sediment in a water tank. Planar flow visualization and particle imaging velocimetry (PIV) simultaneously measured fluid velocities and sediment locations in a radial planar slice of the flow.

2.1 Experimental Setup

For this research, rotor-induced sediment mobilization was modeled in a small scale facility. The small-scale system was composed of a model rotor, ground plane, and sediment bed. These were placed in a tank of water, which acted as the fluid phase in place of air. The higher density and viscosity of water (compared to air) allow for experimentation in a different range of similarity parameter values. Compared to a similar experiment in air [19,22], using water leads to a sediment-to-fluid density ratio further from that of a full scale case, but a terminal-to-characteristic velocity ratio that is much closer. The primary reason for using water instead of air as the fluid phase is that PIV seeding and illumination is much simpler for the higher density fluid due to the availability and higher reflectivity of neutrally buoy-

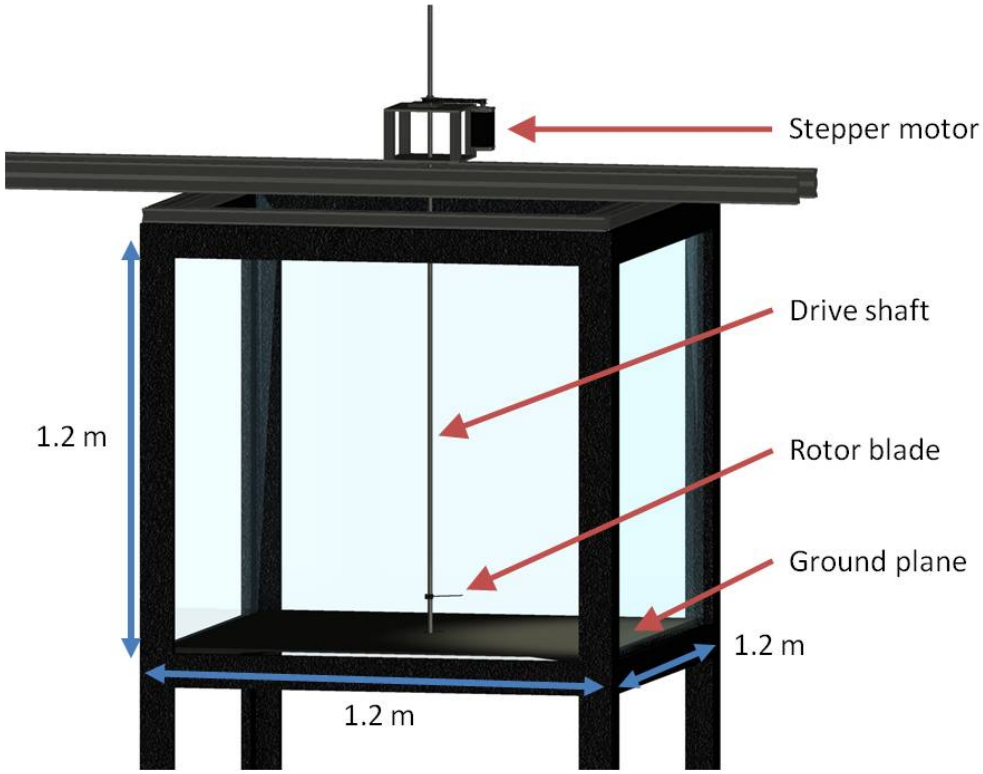

Figure 2.1: Water tank used to simulate rotor-induced sediment mobilization

ant tracer particles. For this experiment, using water as the carrier phase allowed for a larger field of view and lower rotor speeds (and consequently, higher temporal resolution).

The water tank, shown in Fig. 2.1, is 1.2 m (4 ft) on each side. It is made of acrylic windows supported by a steel frame. The windows allow access for optical measurement techniques. The bottom of the tank contains a support bearing for the rotor system, so a false floor was added to provide a level ground plane.

The rotor was single-bladed with a balancing weight opposite to the blade. The blade was milled from aluminum for resistance to corrosion in water. The blade extended 85 mm from the axis of rotation, with a constant chord of 15 mm,

Figure 2.2: Rotor blade

12 degree pitch, no twist, and camber defined by an arc of radius 2.8 cm. This blade is shown in Fig. 2.2. This rotor was designed to match one used in previous research [16]. The rotor was placed one radius above the sediment bed, and was horizontally centered in the tank. The tip of the rotor and the wall were separated by seven rotor radii when the blade was normal to the wall. The blade was covered in a water resistant, minimally reflective coating (matte black spray paint). This paint minimizes reflections from the laser during operation, which is important for safety and decreases interference in the PIV measurements.

The rotor was attached to a ½ in diameter steel drive shaft which was powered via sprockets by a stepper motor (an Omega HT23-600D). The stepper motor enabled accurate control of the rotor speed during data collection. The motor was controlled by LabView^{TM} software using a program written specifically for the operation of these experiments. To minimize stress on the motor, the software signaled the stepper to gradually accelerate to the specified rotational rate and to return

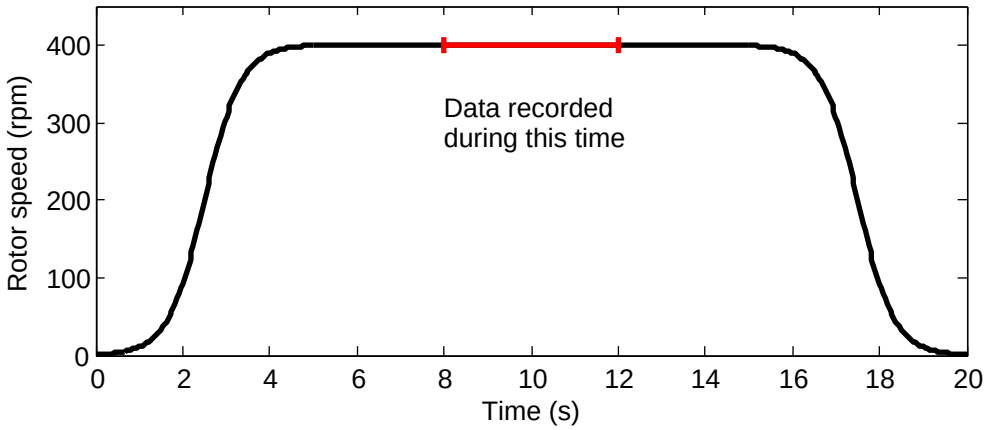

Figure 2.3: Rotor speed versus time

to rest after the data collection. Higher acceleration rates increased the severity of the startup vortex, which in some cases eroded the sediment bed prior to the start of the data collection. Lower acceleration rates increased the time of operation before the rotor reached the specified speed, which also led to sediment bed erosion. After repeated trials and adjustments, a compromise was struck which minimized these effects. Figure 2.3 shows an example velocity profile used for these experiments. Three different types of sediment particles were used during these tests. The particles were each well characterized and spherical, but varied from each other in diameter and density. Because of these differences, the threshold friction velocity and terminal velocity for each sediment was different.

The first sediment used was stainless steel particles 50 µm in diameter. These characterized particles were obtained from Carpenter Powder Products, where their originally intended purpose was fabrication by injection molding. The next sediment type was 54 µm diameter glass particles. The third sediment was 98 µm diameter glass particles. Glass microspheres are produced for a large variety of applications.

Table 2.1: Sediment characteristics [19, 22]

Parameter	Sample 1	Sample 2	Sample 3
Material	Steel	Glass	Glass
Diameter (µm)	50	54	98
Density ($\mathrm{kg\,m^{-3}}$)	7473	2575	2575
Terminal velocity ($\mathrm{mm\,s^{-1}}$)	8.1	2.1	7.4
Threshold friction velocity ($\mathrm{mm\,s^{-1}}$)	6.1	3.6	5.0

The glass particles used here were sieved and characterized for previous work [22]. The varied densities and diameters of these particles allowed for testing multiple values for terminal velocity and threshold friction velocity. Estimated sediment characteristics are given in Tab. 2.1. In addition to the sediment characteristics, test cases in this work varied by rotor speed. The rotor was operated at speeds between 40 rpm and 600 rpm. The full test matrix is available in Tab. 2.2. The Reynolds numbers provided are measured at the rotor blade tip and are relative to the blade chord.

Table 2.2: Cases of rotor-induced sediment mobilization studied for this thesis

Rotor speed (rpm)	Reynolds number ($\times 10^4$)	Particle material	Particle diameter (µm)	Num. trials
40	0.53	Glass	98	2
50	0.67	Steel	50	2
60	0.80	None	–	1
80	1.07	Glass	98	3
100	1.34	Steel	50	3
120	1.60	Glass	54	3
120	1.60	Glass	98	3
160	2.14	Glass	98	4
200	2.67	Glass	54	5
200	2.67	Glass	98	4
225	3.00	Steel	50	7
225	3.00	Glass	98	3
250	3.34	Glass	54	4
250	3.34	Glass	98	3
262.5	3.50	Steel	50	2
265	3.54	Glass	98	3
285	3.81	Glass	98	3
300	4.01	Steel	50	7
300	4.01	Glass	54	1
300	4.01	Glass	98	3
350	4.67	Glass	98	2
400	5.34	Steel	50	4
500	6.68	Steel	50	4
600	8.01	Glass	98	1
600	8.01	Steel	50	3
600	8.01	None	–	1

2.2 Measurement Techniques

PIV was performed to acquire time-resolved velocity fields for a radial slice of the rotor-induced flow. Images were recorded by a four megapixel CMOS camera, a Phantom V641. The camera recorded image pairs of 1600×2560 pixels at a specified rate of 250 Hz. Each image in the pair was separated by 500 µs. This time separation was chosen based on the spatial resolution of the optics and the expected flow velocities [23]. The field of view was illuminated by a dual-head Nd:YLF laser. This laser produces laser light at 1053 nm wavelength which is frequency-doubled to 527 nm visible, green light. The system contains two lasers which enables the capture of minutely spaced PIV image pairs. The emitted beam is passed through a Powell lens, which refracts the beam into a laser sheet. A simple cylindrical lens produces a laser sheet with a Gaussian intensity distribution around the beam axis, while a Powell lens produces a laser sheet with a more uniform intensity distribution. The PIV system is shown relative to the experimental setup in Fig. 2.4. This arrangement was chosen to match previous experiments [19].

The region of interest was chosen to contain the impact of the tip vortices on the sediment bed and to maximize the spatial resolution of the optics. The view extended from the ground plane to 0.1 radii below the rotor, and from 1.15 to 2.7 radii horizontally from the axis of rotation (see Fig. 2.5). The corresponding physical width for each pixel is then 50 µm. The rotor-induced flow is nominally

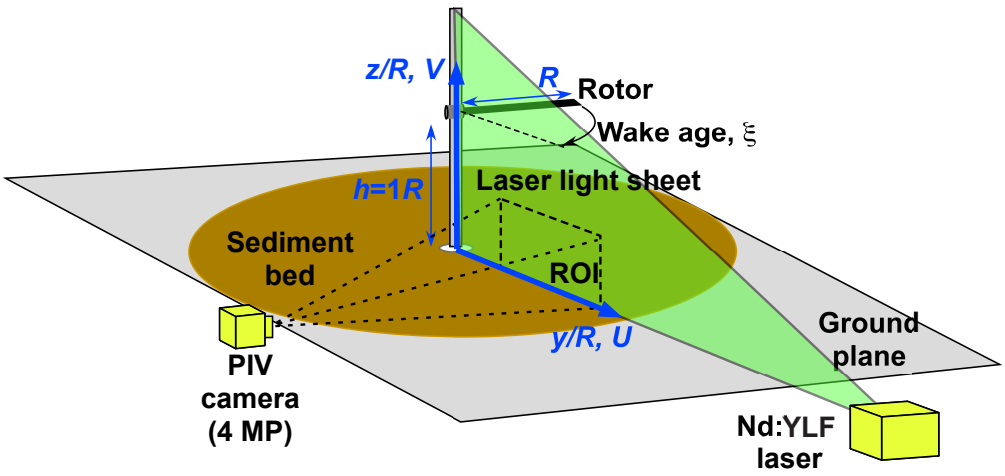

Figure 2.4: Arrangement of equipment for PIV measurement. Adapted from [19]

axisymmetric, so the plane of illumination was chosen to be parallel to one of the tank windows. The camera was then placed perpendicular to the refractive interface to minimize image distortion.

2.3 Particle Imaging Velocitmetry

Each velocity field is made from a pair of images captured in very quick succession [23]. The images are divided into a grid of interrogation regions. The mean planar velocity in each interrogation region is determined by finding the displacement of particles visible in the region. This displacement is determined by the two-dimensional cross-correlation (carried out using fast Fourier transformation) of the pixel values in the region. Conducting this correlation for each interrogation region results in a two dimensional velocity field spanning the field of view. Figure 2.6 shows a schematic of this process.

The flow observed in this experiment was multi-phase. The PIV is intended to measure the velocities of the tracer particles (and thus the velocity of the carrier fluid phase), and not the dispersed phase. This carrier phase isolation is especially important for cases with larger sediment, for which the dispersed phase particles are more likely to be traveling along a different path than the carrier phase fluid. Addi-

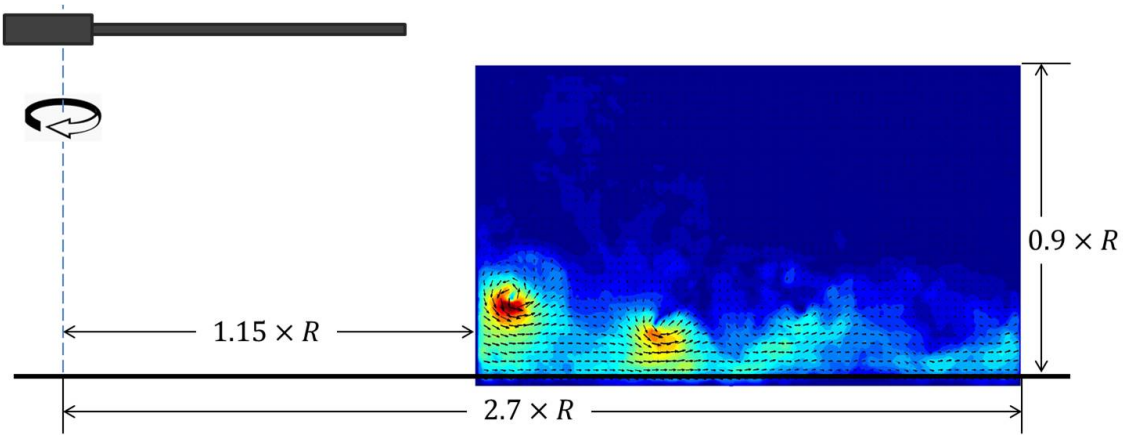

Figure 2.5: Recorded field of view relative to the rotor

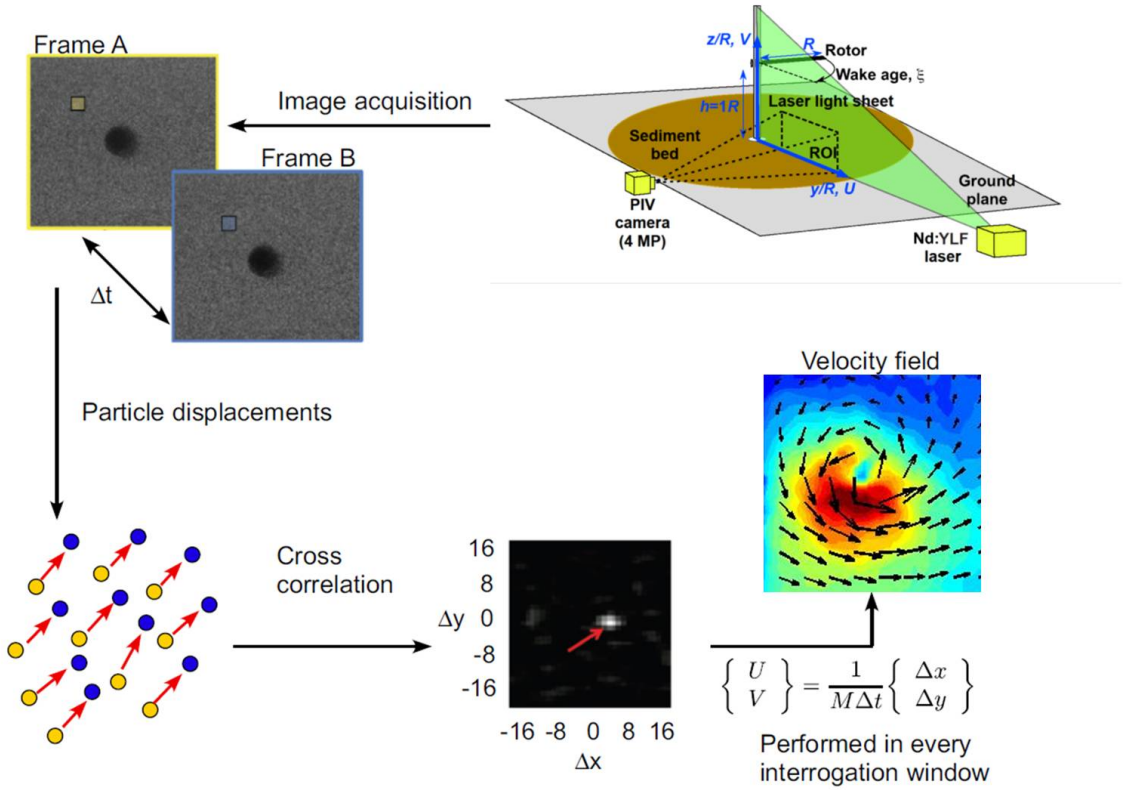

Figure 2.6: Diagram of process for particle imaging velocimetry. Adapted from [22]

tional steps must be taken to minimize the influence of the dispersed sediment phase on the correlations in the PIV processing. For this thesis, carrier phase isolation was accomplished using a multi-pass method, for which the interrogation region width decreased considerably between calculations. The first iteration of PIV inspected large interrogation windows. Although the sediment particle images are much larger than the tracer particle images, the relative quantities of each (many more tracer particles than sediment particles) in a larger window diminishes the influence of the sediment phase on the correlations. The second iteration of PIV inspected small interrogation regions, but shifted the second region by the displacement calculated during the first iteration. This method reduces the influence of the dispersed phase and therefore more reliably measures the velocities of the carrier phase.

For this thesis, the image pairs were separated by 500 µs, and image pairs were recorded at 250 Hz for 4 seconds. This arrangement resulted in 2000 images which make up 1000 velocity fields. PIV recording and processing was carried out using DaVis software. The first velocity measurements were made using 64×64 pixel interrogation windows with 50% overlap. These results were smoothed using a local median filter and used to predict velocities for the second pass. The second set of measurements were made using 16×16 pixel interrogation windows with 50% overlap. These results were not smoothed, but outlier removal was used to replace vectors which varied significantly from neighboring vectors. The spatial resolution of the final vector field is one vector per 407 µm.

2.4 Data Analysis

2.4.1 Sediment quantification

For this research, the severity of the sediment cloud that developed in the rotor wake was quantified by counting the number of mobilized sediment particles in each image. This approach is conceptually simple; a greater quantity of sediment particles suspended in the rotor wake can be interpreted as a more severe example of brownout. Each data set consists of 2000 images, but is only assigned one value to quantify sediment mobilization. For this thesis, that quantity is taken as the mean of the observed number of mobilized sediment particles per image.

It is important to recognize that while this quantification is intuitive, it is not fully representative of brownout severity. As indicated previously by Milluzzo and Leishman [3], sediment clouds resulting from different helicopters can vary significantly in shape. In cases where the suspended sediment is thrown radially far from the helicopter, the danger caused to the helicopter and crew is less than in cases where the sediment remains nearby. This is true even if the number of mobilized sediment particles is the same in each case. Observing a small, fixed field of view in the brownout cloud will result in different sediment uplift measurements based on cloud shape. Comparing brownout severity for different platforms will require some means of addressing these differences. For this research however, only one rotor is used. It can therefore be assumed that the sediment cloud shape is similar for all cases. Based on this, the brownout severity for this system can be compared simply

by relating the number of suspended sediment particles visible in the field of view from case to case. The influence of brownout cloud shape does cause this method of quantification to vary with changing field of view. This limitation will be discussed more thoroughly at the end of this report. The field of view was kept the same for all cases tested here.

Additionally, the measurement of sediment uplift here only accounts for a single planar slice of the wake. This measurement is adequate under the assumption that the rotor wake and its effect on the sediment are axisymmetric. As pointed out by Sydney [24], however, the development of a sediment cloud is generally not axisymmetric. Localized plumes of sediment can be seen in the cloud development in both full scale and small scale experiments. These asymmetric events significantly alter the instantaneous sediment presence, and so any time-averaged data must span enough time that momentary asymmetric effects are diminished. While the presence of these events has been demonstrated, no significant discussion of their frequency or duration is available. This makes it difficult to know how long the measurements must continue before the effects are removed, and so the influence of rotor-induced sediment mobilization asymmetry will be assessed based on the repeatability of the measurements made here.

The measurement of sediment presence in each image is accomplished by phase separation of the two-phase PIV images. A similar challenge has been addressed in a variety of contexts, and the method used here was adapted from those works [25, 26]. Each image was pre-processed by calculating and subtracting a minimum background. This background is determined by searching over time through the

entire data set and collecting the minimum recorded value for each pixel. The background values are then subtracted from each image. Background subtraction removes objects in the image that can be caused by irregularities in the camera sensor or by the presence of reflections and illuminations in the camera's field of view.

Once the images are pre-processed, the phase separation begins. Each step in phase separation focuses on an inherent difference between the tracer and sediment particles. The first difference is that the smaller tracer particles reflect less light, and so appear dimmer in the images. This criterion alone is insufficient for phase separation because the sediment particles occasionally appear dim as well. This can happen if the sediment particle is only partially in the light sheet, or if it is shaded by other particles as in a more dense cloud. It is still helpful, however, to remove all image data below a brightness threshold. This removes dim objects from the image, regardless of their size. The next step, as suggested by Kiger and Pan [25], is to apply a spatial median filter to the images. Each pixel value is replaced by the median value of the $M \times N$ neighborhood surrounding it. This process is a form of signal smoothing; it is a two-dimensional low-pass filter. This median replacement removes small objects (smaller than the filter neighborhood) from the image regardless of their brightness.

The next step identifies particle locations. An algorithm developed by Khalitov [27] seeks local maxima in pixel brightness. In particular, the Khalitov function finds locations around which the local curvature of pixel intensity is negative verti-

cally, horizontally, and along both diagonals. Each of these locations represents a Gaussian-like brightness distribution, which is characteristic of the light scattered from a spherical particle. Each Gaussian peak is recorded as a particle location.

Many local maxima identified at this point will not correspond to a unique particle or to a particle at all, but rather to noise peaks or artifacts of the previous processing steps. Each identified peak must be inspected to verify that it corresponds to a sediment particle. This step is made much simpler by the original minimum threshold, which dramatically reduces the number of potential particles to check. The verification process involves an inspection of the size and brightness of each particle. If the pixels surrounding the identified particle location are bright enough on average, and the number of contiguous, bright pixels is high enough, the particle is confirmed as sediment. The threshold values were adjusted until processing a set of sample images matched between manual and automatic particle identification. Specifically, a steel sediment particle was required to occupy at least 14 pixels of the image and have an average pixel value of at least 2700 (out of 4095), and a glass sediment particle was required to occupy at least 9 pixels with an average value above 1000. Figure 2.7 shows an example image region before and after this filtering is applied. In this case, the tracer particles are removed and the sediment remains.

This threshold procedure leaves some uncertainty in the effective measurement volume in which the sediment is identified. The nominally two-dimensional section of the rotor wake that is illuminated by the laser sheet has a finite depth, and variations in that depth will influence the number of visible particles. For ex-

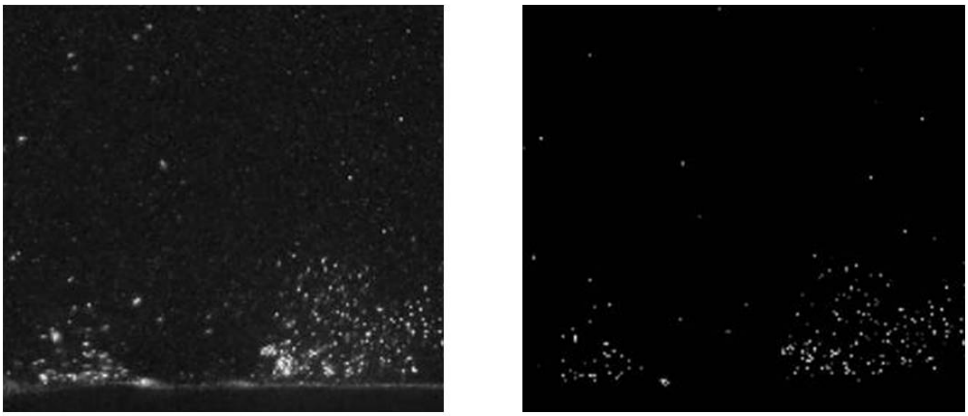

Figure 2.7: Phase separation procedure applied to an example two-phase PIV image

ample, a particle which reflects more brightly may be identified even if it is far out of plane, effectively widening the measurement depth when compared to particles which reflect less. While the absolute volume is not crucial for the current work, the relative volume for each individual sediment type can introduce error in the sediment concentration measurements. This error is minimized by the adjustment of the threshold values, but not removed entirely. An investigation and quantification of this effect is discussed in chapter 3 [28].

This sediment identification described above produces a scalar quantification of sediment mobilization in each image set. However, the Khalitov algorithm does not perform well in cases where the image (or regions of the image) are nearly saturated with particles. In these cases, the individual particles appear smeared together in the image, which eliminates the ability to locate them by inspecting local brightness curvature. This opacity effect caused an apparent decrease in brownout intensity (as indicated by the number of identified particles) at high rotor speeds which was

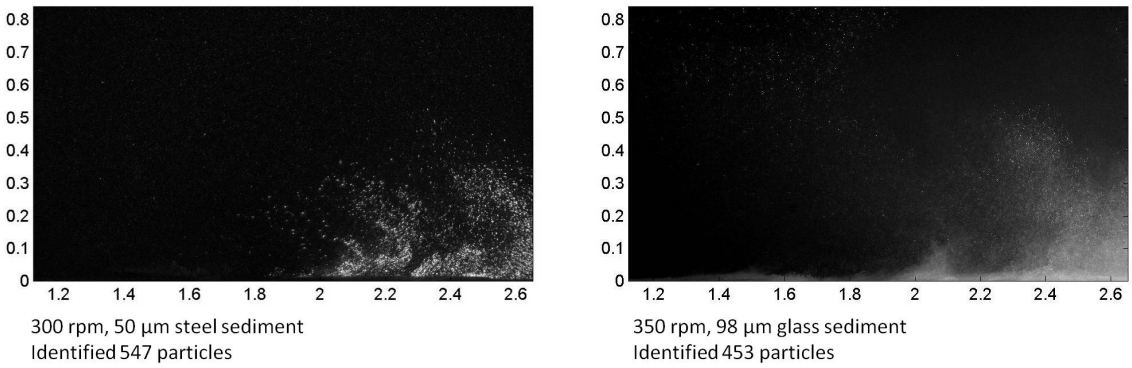

Figure 2.8: Due to excessive optical density, a visible increase in sediment uplift is contradicted by a measured decrease

contradicted by visual inspection of the images. Figure 2.8 shows an example of this phenomenon. Because of this limitation, some of the cases with more severe sediment mobilization were not considered in the remainder of this report. While other methods of quantifying sediment mobilization may have improved success in these regimes, no significant effort was spent inspecting these cases because the same cases are not able to be measured by the PIV procedures either. The same image saturation is referred to as "optically dense" in PIV literature, and is not usable for producing velocity fields. This limitation will be discussed further at the end of this thesis.

2.4.2 Wake characterization

At this point, the sediment quantification procedure has analyzed the images and identified for each data set a single scalar value of sediment uplift. The next step is to compare the measured sediment presence to the characteristics of the wake in each data set. To this end, additional processing is required to identify a set of scalar wake characteristics that adequately describe the flow conditions.

By characterizing the most important features of the rotor-induced flow using a set of scalar values, quantitative comparisons can be made between the flow and the resulting sediment uplift. These scalar characteristics, although not directly controlled in the experiment, will serve as the independent variables in the dynamic scaling investigation of rotor-induced sediment mobilization presented in chapter 3.

2.4.3 Wall jet velocity

The first flow feature to be characterized is the wall jet. The wall jet, the radial flow outward along the ground plane, is the primary flow feature in the time-averaged velocity field (see Fig. 1.5). The wall jet velocity profile is determined from the time-averaged velocity field by averaging the horizontal velocity components at each discrete height in the field of view. This procedure produces a curve of mean horizontal velocity versus height above the ground. The maximum value of this profile is taken as the wall jet velocity.

2.4.4 Vortex measurement

As previously discussed, a time-averaged observation of the flow field, such as the wall jet velocity measurement above, is not on its own a sufficient description of the rotor wake [16]. The periodic passing of rotor tip vortices is the dominant flow feature, and so the vortex properties must be measured to properly characterize the flow.

Two approaches are used to measure the vortices. The first is to locate each vortex in the flow and characterize it directly in terms of its size and shape. These vortices can be characterized by three quantities: core radius, peak swirl velocity, and circulation. The second approach is to indirectly observe the vortices in terms of the effects that they have on the instantaneous wake flow field measurements. This approach is similar to the statistical analysis of turbulence in that the procedure will decompose the wake into mean flow and fluctuations (of which the tip vortices are dominant).

The first step towards direct vortex measurement is finding the vortices in each velocity field. The data in this thesis span 81,000 velocity fields and each contains between 1 and 4 vortices; manual recognition would take too long. A computer can work quickly, but it is non-trivial to automatically identify the relevant patterns. The vortex identification method used here is the Γ_1 function [29]. This equation is applied to a velocity field and produces a scalar field indicating the similarity between the local velocities and a simplified rotational flow. The peaks in this

function indicate the likely locations of vortices. The Γ_1 function is defined as:

$$\Gamma_1 = \frac{1}{N} \sum \frac{P\bar{M} \times U_M}{||P\bar{M}|| \cdot ||U_M||}$$

A schematic of this function is shown in Fig. 2.9. For the vector in the velocity field, P, the Γ_1 function operates on the local area S which contains N other vectors. The size and shape of S are predetermined; for this thesis, S is a circular area centered on P with a radius of 16 vectors (or roughly 6.7 mm, which is 2 to 3 times the measured core radii). For each point M in the region S, the Γ_1 function computes the cross product of the vector connecting that point to the center, $P\bar{M}$, with the flow velocity at that point, U_M. This is normalized by the magnitude of each of those vectors to produce a number between -1 and 1. The value of the Γ_1 function for the point P is the average of each of the normalized cross products in S. The average of these numbers is 0 for exclusively radial flow and ± 1 for exclusively tangential flow. Examples cases are given in Fig. 2.10.

Flow around vortices in a rotor wake includes tangential flow from the vortex and shear flow from top edge of the wall jet. This additional flow can alter the Γ_1 field, and results in a measured vortex center which is above the actual center of rotation. The wall jet's contribution to the flow is removed by subtracting the time-averaged velocity field out of the instantaneous velocity measurements. The Γ_1 function is then applied to the instantaneous variations in velocities. The difference is shown in Fig. 2.11 and the identified vortex center is marked in each image.

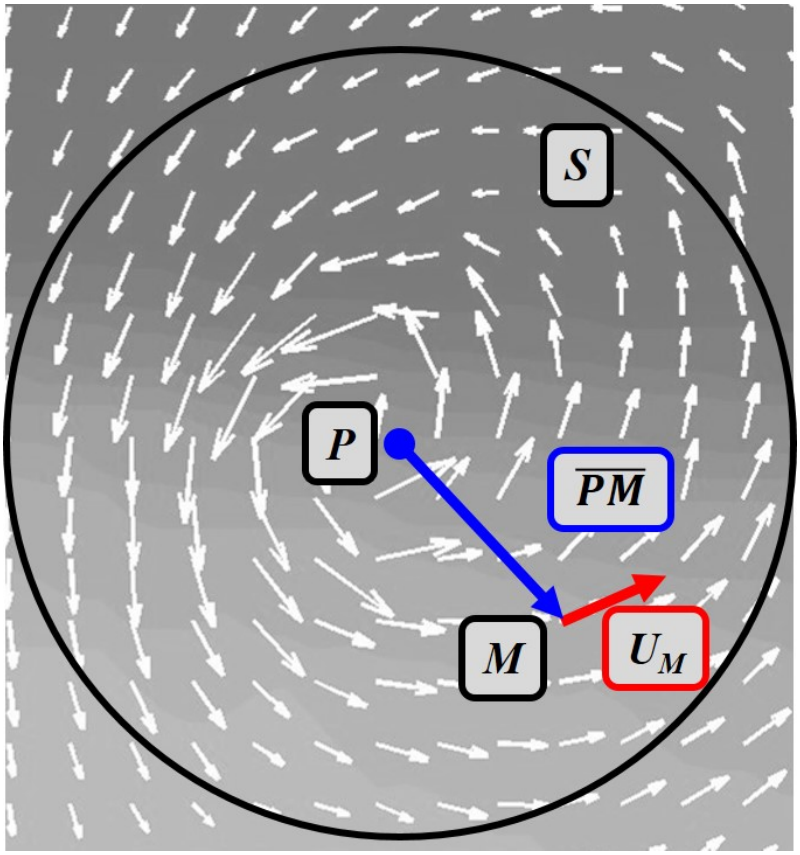

Figure 2.9: Γ_1 function schematic

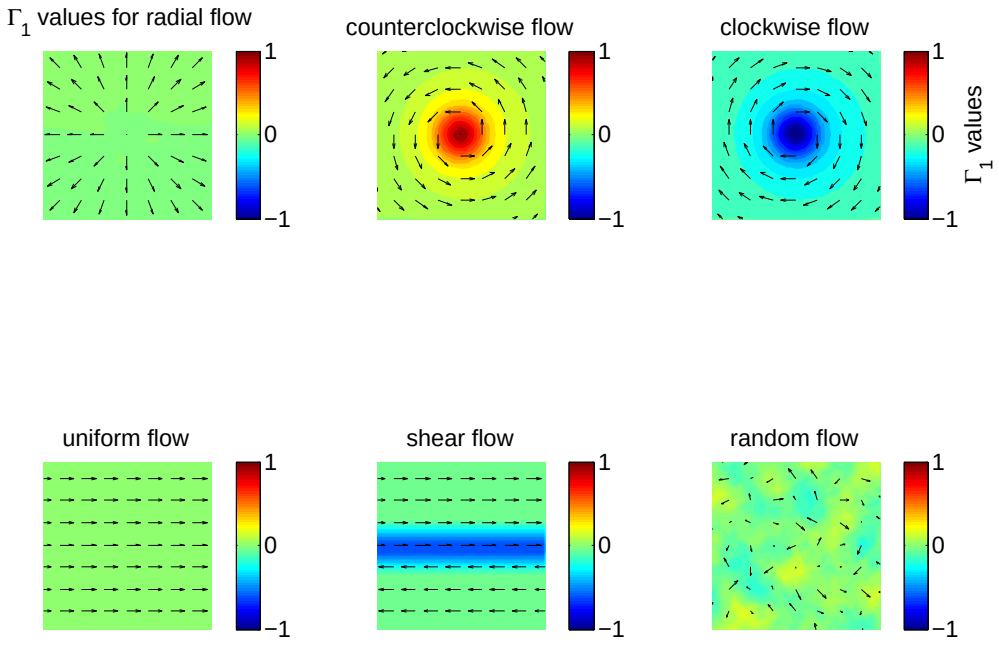

Figure 2.10: Γ_1 applied to example flows

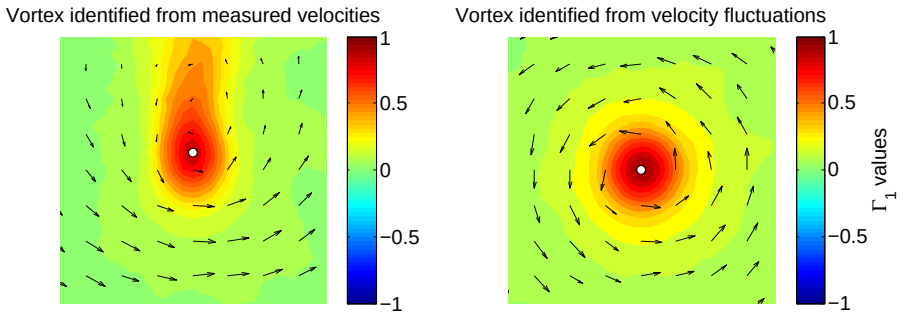

Figure 2.11: Γ_1 applied to instantaneous velocity field and to velocity fluctuations

Some flow structures, such as the shear layers at the top and bottom edges of the wall jet, can create peaks in the Γ_1 function that do not correspond to tip vortices. For a simple search function, these areas are as likely as tip vortices to be identified. If these flow regions were processed as if they were blade tip vortices, the error of the overall vortex characterization would significantly increase. A solution is needed to minimize this error.

To eliminate these misidentified flow structures, individual vortices were tracked over time. Vortices nearer to the blade tip are stronger and more distinct than vortices which have convected, distorted, and diffused as they move through the rotor wake. The Γ_1 function is particularly adept at finding vortices near the blade tip. This location information can be used for each later time step as a means of more accurately locating the vortex as it convects. In the rotor wake studied here, it is known that vortices are generated at the rotor tip, and not elsewhere. From there, they move across the field of view from left to right until they exit the image or diffuse. To take advantage of this information, the Γ_1 function was applied only in the region where vortices enter the field of view and in the locations of vortices from the previous time step. Peaks in the Γ_1 function that appear elsewhere are disregarded in this search.

For a sufficiently high time-resolution (at least high enough that the vortex convection between time steps is less than the radius of area S), the search function can predict the position of each vortex in each new image based on their locations in previous time steps. An adaptive application of the Γ_1 function ensures that the processing identifies exactly one vortex in each of these regions for each time

step. These adaptations are made by changing the threshold Γ_1 function value above which the search interprets a point as a vortex center. If the search originally returns without finding a vortex where one is known to be, the search is modified by reducing the required Γ_1 value. If multiple vortex centers are located, the requirement is increased. Iterative application of this function identifies the location of the vortices present in each measured flow field.

After the vortices are located, they must be characterized. A vortex is a coherent region of rotational velocity in the fluid, which can be described by three quantities: the total circulation contained in the rotating flow, Γ_v, the maximum tangential flow velocity around the vortex center, $V_{\theta\,\max}$, and the vortex core radius, R_c.[1] These parameters characterize the instantaneous size and strength of a vortex.

Empirical and analytical work has shown that vortices have a consistent shape. This shape is represented by a model of the variation in tangential velocity along the vortex radius. These models vary relative to the three vortex characteristics mentioned above. Several vortex models have been used in previous studies, including:

$$\text{Rankine vortex profile:} \qquad V_\theta = \frac{\Gamma_v r}{2\pi R_c^2} \quad (r \le R_c), \qquad V_\theta = \frac{\Gamma_v}{2\pi r} \quad (r > R_c)$$

$$\text{Lamb-Oseen vortex profile:} \qquad V_\theta = \frac{\Gamma_v}{2\pi r}\left(1 - e^{-\alpha\left(\frac{r}{R_c}\right)^2}\right), \qquad \alpha = 1.25643$$

$$\text{“Scully” vortex profile:} \qquad V_\theta = \frac{\Gamma_v}{2\pi}\left(\frac{r}{R_c^2 + r^2}\right)$$

[1] To clarify, Γ_v is a second use of the symbol Γ; it is distinct from Γ_1. Each is related to flow rotation. Before this point, discussion has focused on Γ_1, a function to inspect dominance of rotation in a local flow field [29]. For the remainder of this thesis, more focus will be given to Γ_v, the vortex circulation which quantifies the strength of the flow's rotation.

To evaluate Γ_v, $V_{\theta\,\max}$, and R_c for each of the vortices located by the previous step, a velocity profile model will be fit to the measured velocity profile, and the values will be determined from the equation for that model. The chosen model must therefore best represent the vortices to which it will be compared. Three available models are shown in Fig. 2.12. The Rankine profile assumes a solid body rotation inside the core and an irrotational flow outside. This simple model is useful for analytical work, but does not capture the behavior of a vortex in a viscous flow. The Lamb-Oseen profile is derived from the Navier-Stokes equations for two dimensional flow and thus models a viscous core. Because of this, the Lamb-Oseen model more accurately represents the physical traits of a vortex. The Scully profile algebraically approximates the Lamb-Oseen model. It is far less computationally expensive and only slightly less accurate. This compromise is especially useful in numerical simulations, in which the calculation must be made many times. Since computation time was not a limiting factor here, the Lamb-Oseen model was used.

From the local velocity data around each vortex center, tangential velocity components were plotted against radial distance. The inspected region was set to be up to 5 times the estimated core radius from the vortex center, but was restricted to not continue past the ground plane or include flow around any other vortex. This added limitation was especially important in the high rotor speed cases, for which neighboring vortices were quite near to each other.

The data for each identified vortex was fit with the curve defined by the Lamb-Oseen model of vortex flow as shown in Fig. 2.13. By finding the best fit parameters for the Lamb-Oseen model to this data, each vortex's core radius, peak tangential

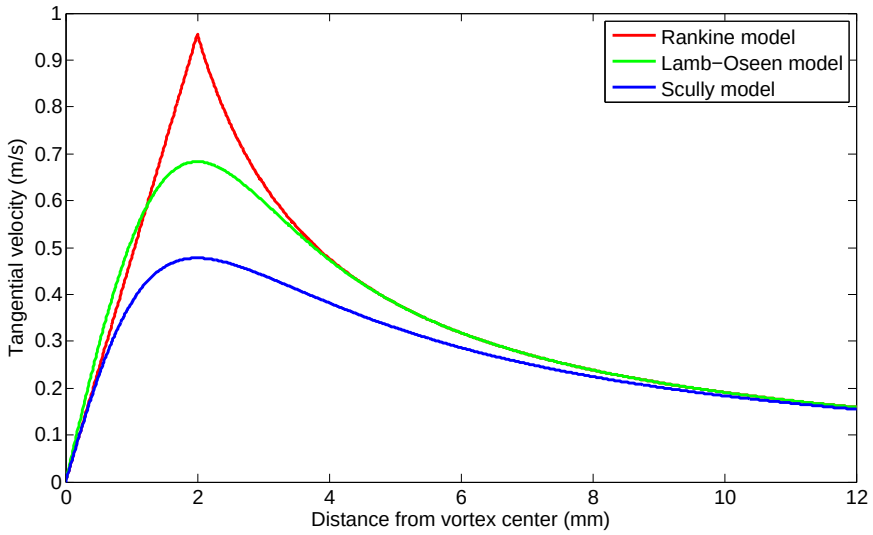

Figure 2.12: Vortex velocity profiles. $\Gamma_v = 0.012\,\mathrm{m^2\,s^{-1}}$, $R_c = 2\,\mathrm{mm}$.

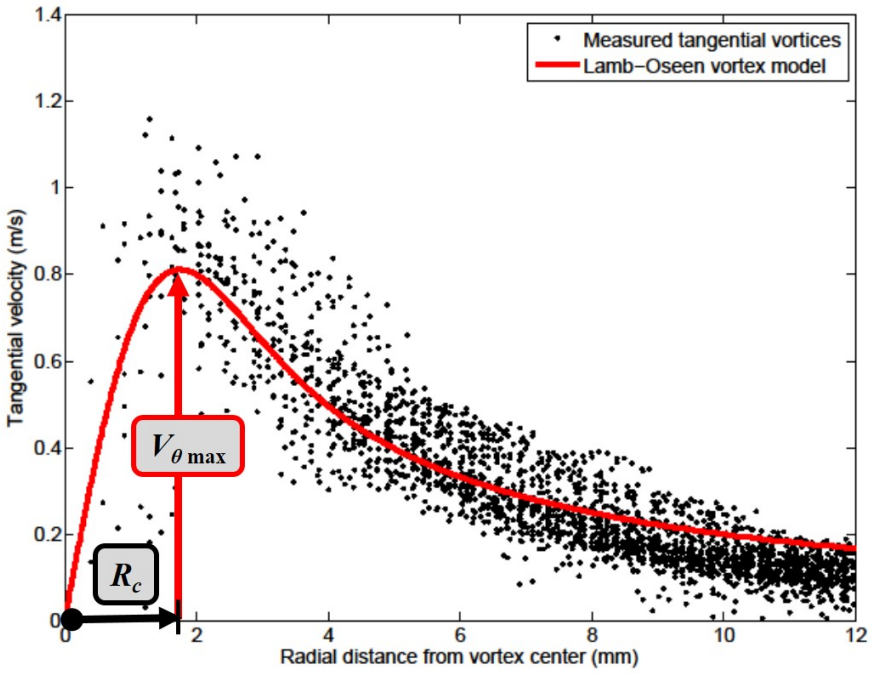

Figure 2.13: Lamb-Oseen model fit to measured data

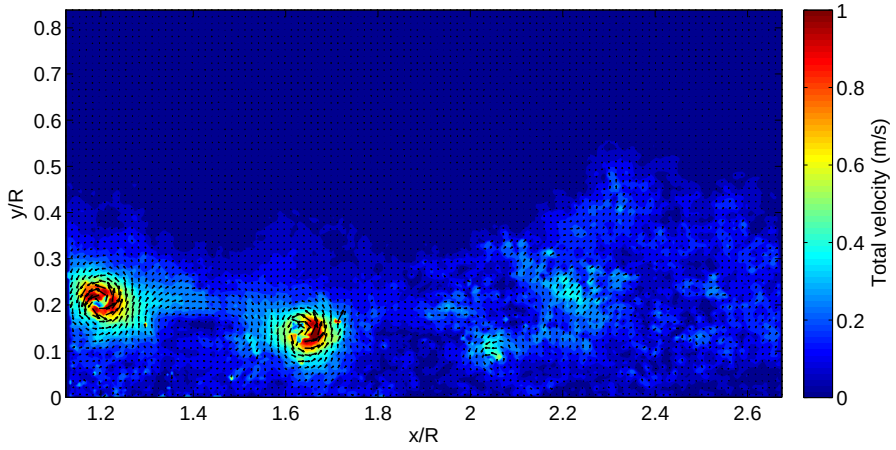

Figure 2.14: Instantaneous velocity fluctuations from time-averaged flow

velocity, and circulation were determined. Once each vortex was assigned its best-fitting value of Γ_v, $V_{\theta\,\max}$, and R_c, each case in the test matrix (Tab. 2.2) was characterized by the mean value of those vortex characteristics over all vortices in that data set.

2.4.5 Turbulent kinetic energy

An alternate method of wake characterization can be adapted from turbulence analysis. Because the tip vortices are the dominant unsteady flow feature in the rotor wake, the instantaneous velocity fluctuations from the time-averaged wake (as in Reynolds decomposition) can be treated as directly related to the influence of the vortices. The instantaneous and time-averaged velocity fields have been shown previously (Figs. 1.4 and 1.5). Figure 2.14 shows the difference between these, the instantaneous velocity fluctuations.

Calculating the turbulent kinetic energy, k, does not require the identification of individual vortices. This simplification reduces the effort required significantly, and is the primary advantage of this approach. The kinetic energy was calculated per unit depth and per unit mass for each vector in each of the N velocity fields, given by:

$$k = \frac{1}{N} \sum_{i=1}^{N} \frac{1}{2}((u_i - \bar{u})^2 + (v_i - \bar{v})^2)$$

Here, u_i and v_i indicate the instantaneous velocity measurements while $\bar{u}$ and $\bar{v}$ represent the time-averaged velocities. The values of k are averaged over the entire field of view to evaluate the mean turbulent kinetic energy contained in the region of interest.

2.5 Summary

The procedure used in this thesis for the characterization of rotor-induced flow and the resulting sediment mobilization severity was described. Sediment mobilization was quantified by identifying the number of visible particles in each of the two-phase PIV images. These images were filtered using a local median filter and the Khalitov search function to isolate the dispersed phase from the tracer particles in the carrier phase. The rotor wake was characterized in terms of the blade tip vortices. Vortex locations were identified and tracked using the Γ_1 function. Vortex size and strength were determined by fitting the Lamb-Oseen vortex velocity profile

to measurements of the local flow velocity. Vortex circulation, peak swirl velocity, and core radius were determined using this model-fit procedure. The rotor wake was also characterized in terms of turbulent kinetic energy and wall jet velocity.

Chapter 3: Results and Discussion

This chapter presents the results achieved by the procedure described in the chapter 2. All of the data presented below was extracted from sets of dual-phase PIV images, an example of which is shown in Fig. 3.1. This image was taken from a data set recorded for a rotor speed of 400 rpm and using 50 µm steel sediment. This example case will be used to present each step of the results. The discussion of the results will be divided into carrier phase flow characterization and dispersed phase quantification. After the measurements are discussed, an analysis of system dependencies will be presented.

3.1 Carrier Phase

The result of time-resolved PIV was a time-series of planar velocity measurements for a radial field of view within the rotor-induced flow. To characterize the flow in a small set of scalar parameters, these velocity fields were separated into the dominant flow structures: the wall jet and blade tip vortices. Each of these structures was measured and used to more thoroughly describe the flow conditions.

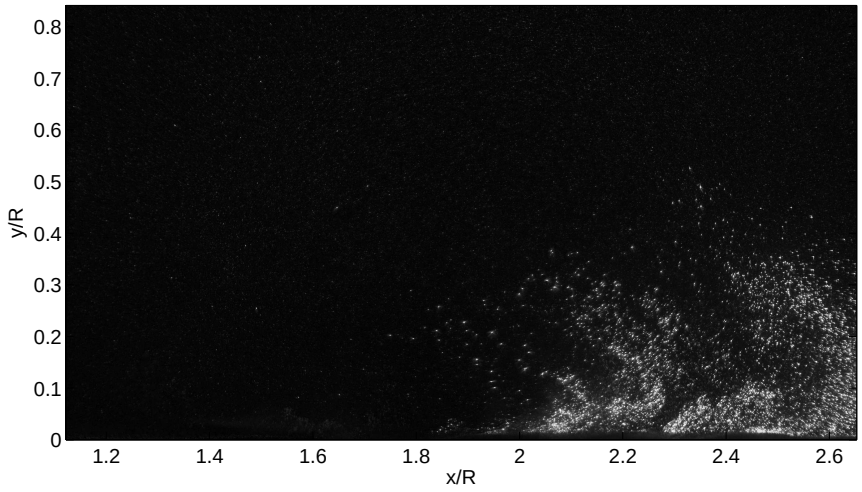

Figure 3.1: A sample PIV image. The sediment here is 50 µm steel particles, and the rotor is spinning at 400 rpm.

Processing the image in Fig. 3.1 (and its PIV image pair) produces the velocity field shown in Fig. 3.2. This vector map is an instantaneous[1] measurement of the in-plane velocities in the rotor wake. Figure 3.3 shows the time-averaged flow field for the same data set, and Fig. 3.4 shows the instantaneous velocity fluctuations (the difference between the previous two figures). Velocity fields like these are the basic measurements from which all of the following wake characteristics were extracted.

Both the tip vortices and wall jet are visible in the instantaneous velocities (Fig. 3.2). The steady wall jet is more easily visible in the time-averaged velocities (Fig. 3.3), which does not show the vortices. Conversely, the tip vortices are more easily visible in the velocity fluctuations (Fig. 3.4), which does not show the wall jet. The vortices are generated at the rotor blade tip, which is at the coordinate

[1]No measurement technique is truly instantaneous. PIV measurements deduce local velocities based on two discrete position measurements. The measured velocity is therefore an average over the time between the images, in this case 500 µs. For the relevant time scales here (the vortices in this study pass once every 100 ms at most), this is fast enough to be considered instantaneous.

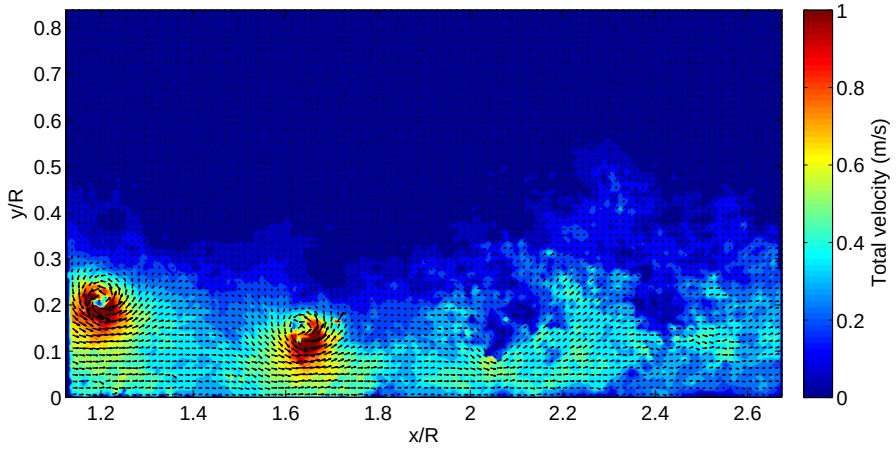

Figure 3.2: Instantaneous velocity field for rotor wake in ground effect. 50 µm steel particles, 400 rpm.

(1,1) on the rotor-normalized axis, so the vortices further to the left are closer to the rotor. The vortex closest to the left edge was generated most recently, and so is the most concentrated and most prominently visible. The vortex furthest from the left edge has diffused significantly, and is not readily visible in the velocity field.

Even the vortices which are difficult to identify by looking at Fig. 3.4 can be found using the Γ_1 function. Figure 3.5 shows the Γ_1 function value for each point in the field of view. Note that the Γ_1 search window cannot pass the data's edge, which creates a border of unmeasured vectors. The width of the border is equal to the radius of the interrogation window, S. This border causes a slight reduction in the effective field of view. In Fig. 3.5, the vortices are visible as areas of high Γ_1 values. The regions of Γ_1 near -1 are rotating opposite to the direction expected for a blade tip vortex, and so are not considered here. For reference, the peak Γ_1 value for the left-most vortex here was 0.92.

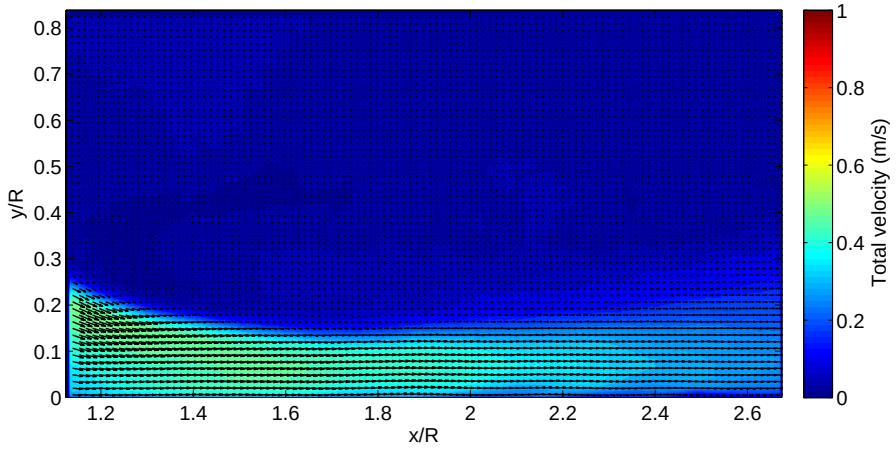

Figure 3.3: Time-averaged velocity field for rotor wake in ground effect. 50 µm steel particles, 400 rpm.

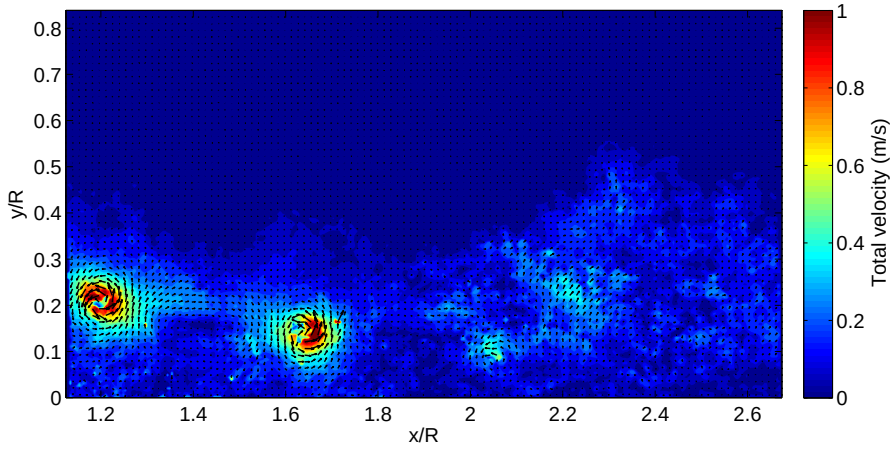

Figure 3.4: Instantaneous velocity fluctuations for rotor wake in ground effect. 50 µm steel particles, 400 rpm.

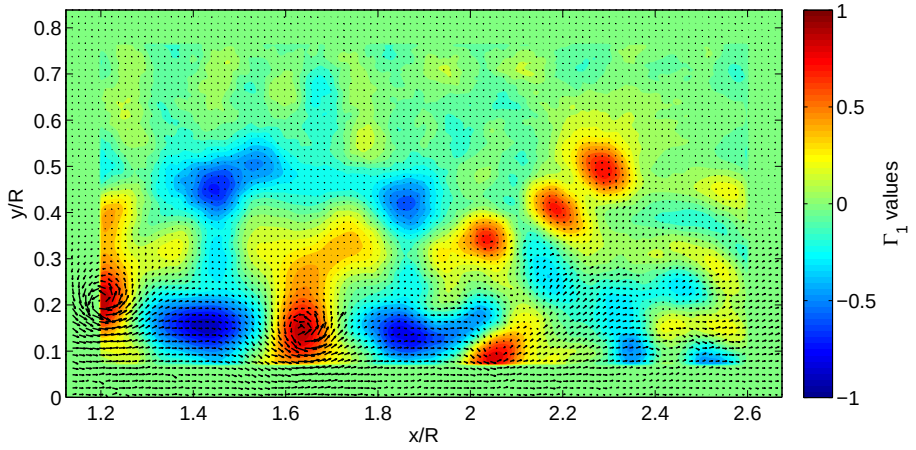

Figure 3.5: Γ_1 field for rotor wake in ground effect. 50 µm steel particles, 400 rpm.

Not every peak in the Γ_1 function corresponds to a rotor blade tip vortex. Figure 3.5 contains 6 peaks that could correspond to tip vortices. The accuracy of vortex identification was improved by tracking vortex movement in time. For the same example data, the vortex centers and their paths over time are displayed in Fig. 3.6. These data show that only 4 of the 6 peaks are tip vortices. The right-most vortex in Fig. 3.6 has risen above the wall jet because of interactions with another vortex.

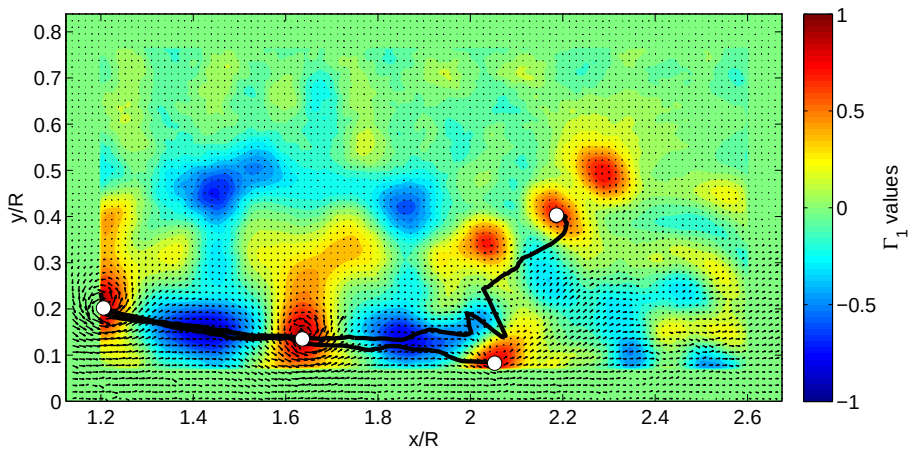

Figure 3.6: Γ_1 field with vortex locations and paths marked. 50 µm steel particles, 400 rpm.

3.1.1 Vortex measurement

In the next step of carrier phase processing, measurements were made of the vortex characteristics by fitting the Lamb-Oseen vortex model to the measured velocity profiles. The velocity profile of the left-most vortex visible in Fig. 3.6 is shown in Fig. 3.7. The tangential velocity components are plotted versus the radial distance from the vortex center.

From this velocity profile (and many more like it), the vortex characteristics of circulation, peak swirl velocity, and core radius can be extracted from the best fit Lamb-Oseen model. In this case, the model that fit most closely to the measured profile was

$$V_\theta = \frac{12.5}{2\pi r}\left(1 - e^{-\alpha\left(\frac{r}{1.8}\right)^2}\right)$$

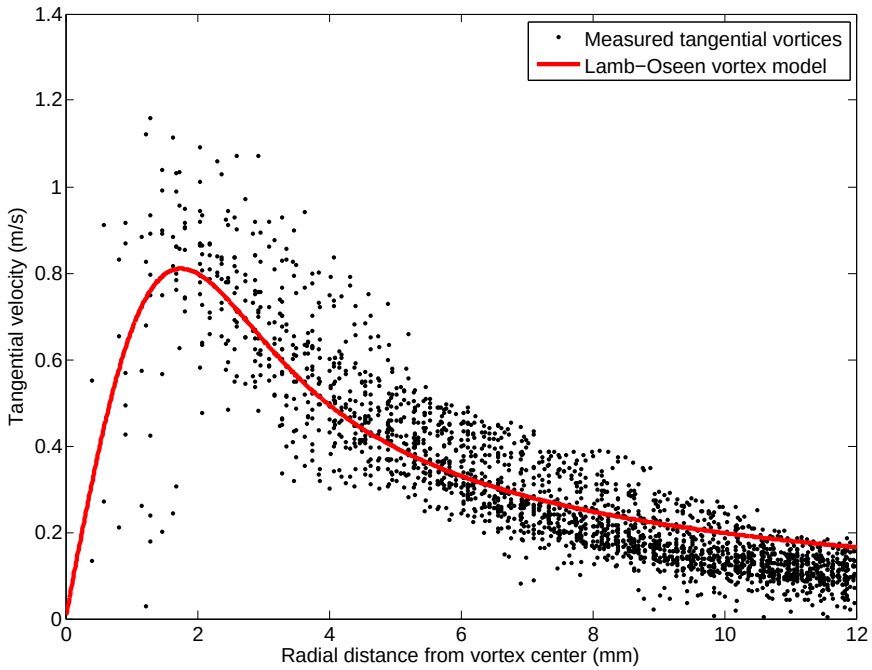

Figure 3.7: Example vortex velocity profile

For this individual vortex, the values of $\Gamma_v = 0.0125\,\mathrm{m^2\,s^{-1}}$, $V_{\theta\,\max} = 0.81\,\mathrm{m\,s^{-1}}$, and $R_c = 1.8\,\mathrm{mm}$ are found from the Lamb-Oseen model fit. For this curve, $R^2 = 0.79$.

These three vortex parameters are the primary wake characteristics that will be compared to the quantity of sediment uplift. It is therefore especially important to reduce the error associated with their quantification. The error in the fit can be connected to the R^2 goodness-of-fit statistic for each curve:

$$R^2 = 1 - \frac{\sum_i (y_i - f_i)^2}{\sum_i (y_i - \bar{y})^2}$$

Inspection of the goodness-of-fit of the Lamb-Oseen model to local velocity profiles for each vortex showed that there were many poorly fitting curves. Figure 3.8 shows a histogram of the R^2 statistic over all of the measured vortices. Many of these measurements resulted in low R^2 values. Further investigation revealed

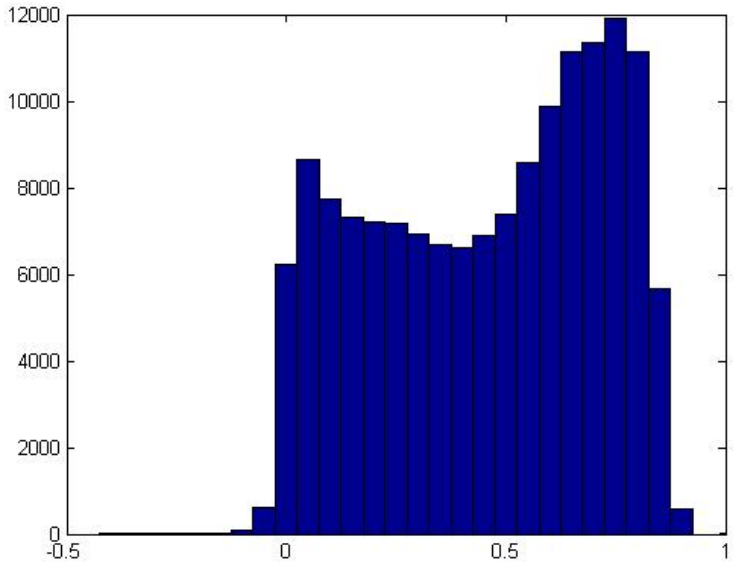

Figure 3.8: R^2 histogram for all measured vortices

that the occurrence of poorly fitting curves correlated strongly to the top and right regions of the field of view. The top region of the field of view is above the wall jet, and a vortex rarely ends up above the wall jet. Most of the data in this region corresponds either to vortices distorted by another vortex or to regions of vorticity from the shear layer. The right edge of the field of view contains mainly aged and diffused vortices, which do not lend themselves to quantification by curve fitting. In both cases, the Lamb-Oseen model is not able to characterize the vortices since they are no longer shaped as the model predicts. Figures 3.9 and 3.10 show the goodness-of-fit statistics for measurements made inside and outside of the suspect regions. As expected, the vortices which are above the wall jet or far from their origin at the rotor display low R^2 values. The remaining measurements display much higher R^2 values. Removing these regions from the data eliminates the bulk

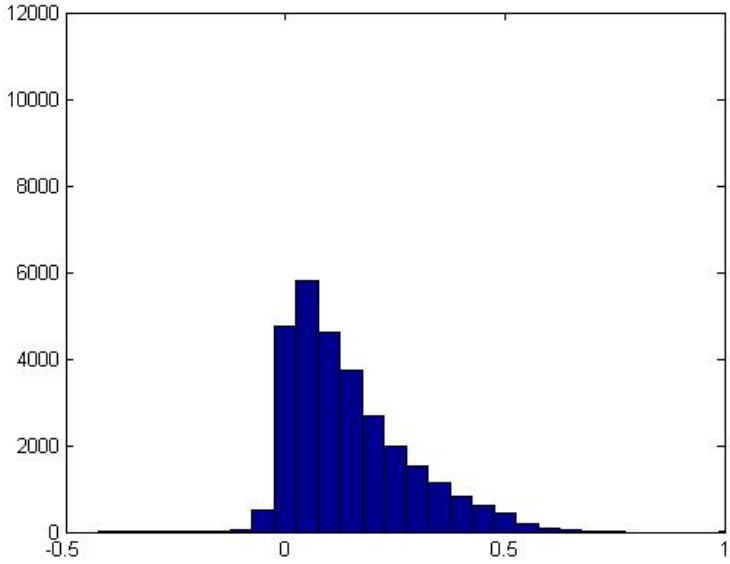

Figure 3.9: R^2 histogram for measurements which were removed based on location

of the poorly fitting curves. Additionally, data measured within the central region which still resulted in an R^2 value below 0.4 were discarded. This again slightly reduced the effective field of view.

Each test case was then characterized by the average of all vortices contained within it.[2] It is expected that each of these parameters is dependent on rotor speed in some way. Plotting each of the vortex characteristics versus rotor speed can verify this dependency. This inspection can also reveal whether the presence and type of sediment had any significant effect on the wake characteristics. If the data for different sediment types all collapse to a single trend, then the presence of sediment did not significantly alter the vortex characteristics. Figures 3.11-3.13 show the

[2]For this thesis, PIV image pairs were recorded at 250 Hz, resulting in 4 seconds of data collection. This timing was the same for all data sets. Because of this, the number of vortices which passed through the field of view in this time was proportional to the rotor speed. For example, when the rotor operates at 300 rpm, 20 vortices pass during the 4 seconds of data collection. When the rotor operates at 120 rpm, only 8 vortices pass in 4 seconds.

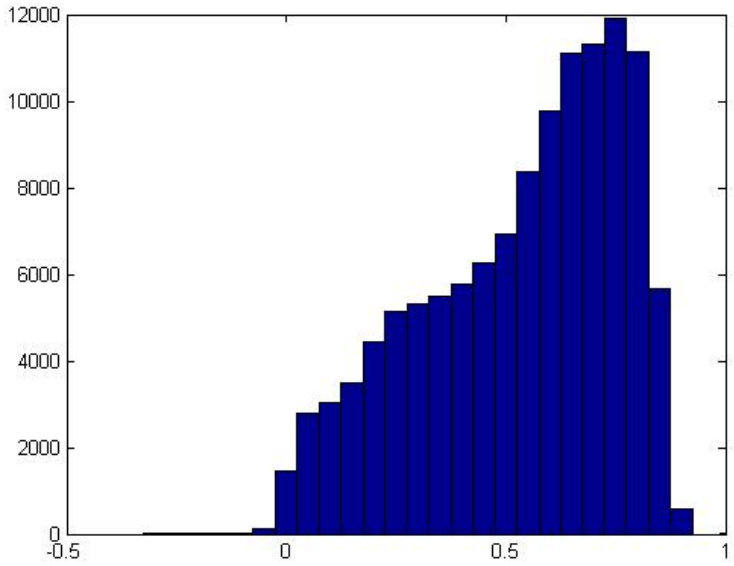

Figure 3.10: R^2 histogram for measurements which were retained based on location

trends of vortex circulation, peak swirl velocity, and core radius each versus rotor speed. Data points on these plots are colored to indicate which sediment was present in the corresponding data set.

The circulation increases linearly with the rotor speed. The various sediments do not seem to alter the vortex circulation. This agrees with expectations based on bound circulation theory. Similarly, the trend of vortex peak swirl velocity is nearly linear at low rotor speeds and is not noticeably changed by the sediment characteristics. At rotor speeds above 400 rpm, however, the previously linear trend appears to become nearly level. This is potentially an effect of increased vortex diffusion at the higher rotor speeds. This diffusion would effectively smooth the velocity profile, causing a decrease in the peak swirl velocity.

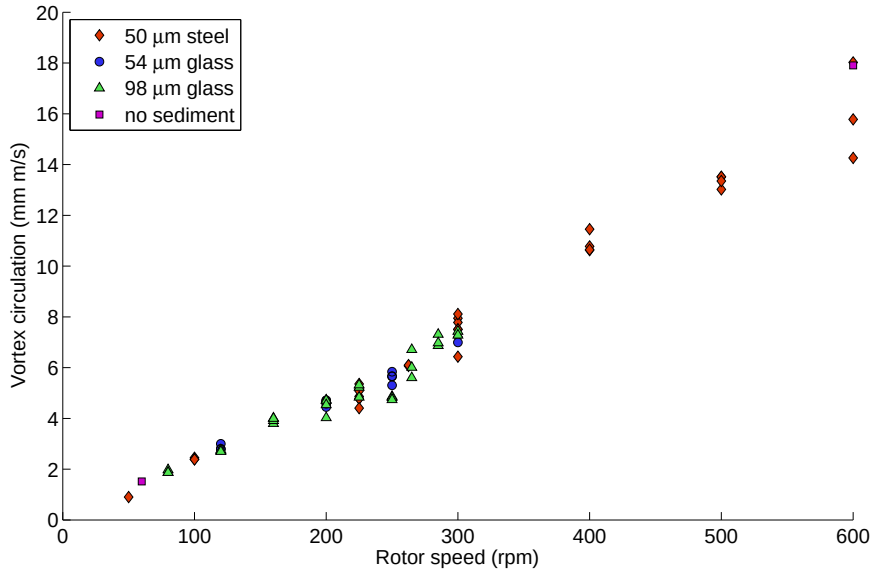

Figure 3.11: Vortex circulation measurements

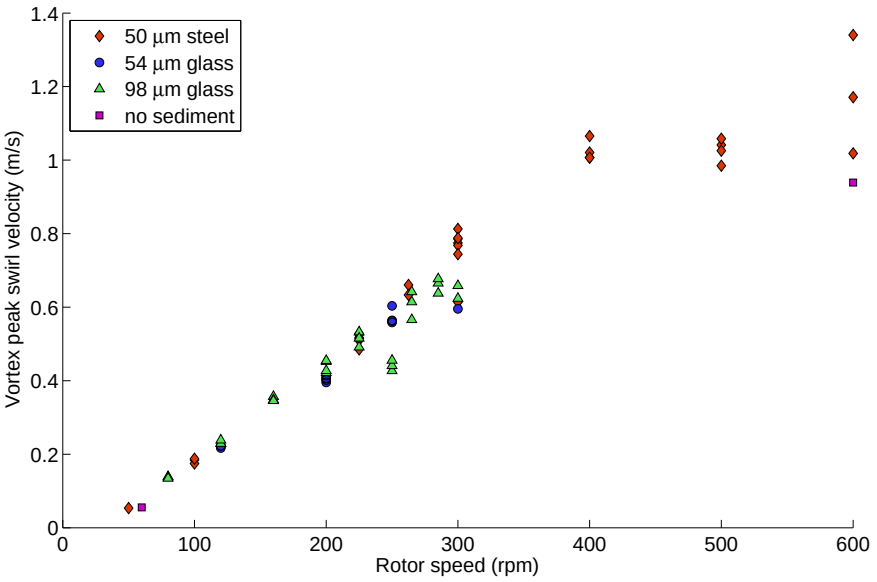

Figure 3.12: Vortex peak swirl velocity measurements

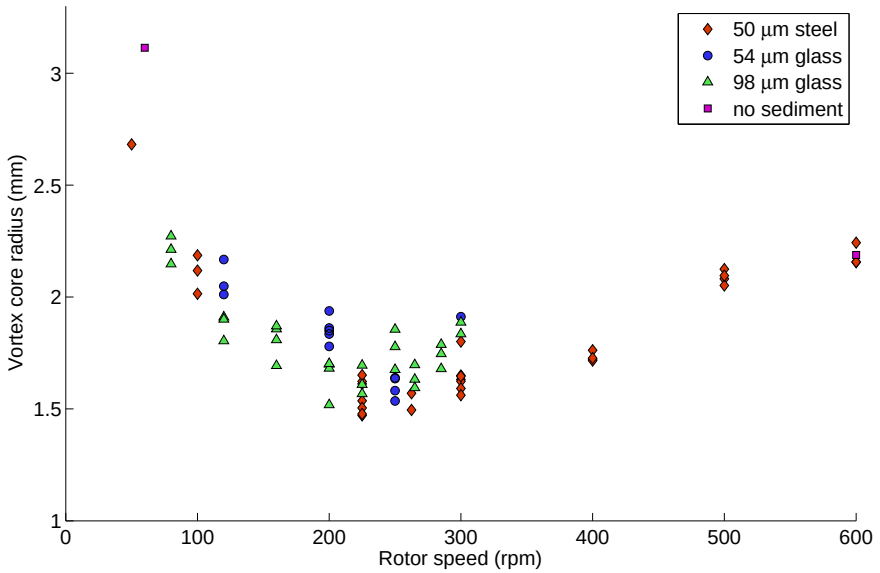

Figure 3.13: Vortex core radius measurements

The third characteristic measured here, the vortex core radius, does not follow a linear trend. Again, the data from each sediment type falls on a single trend, indicating that the sediment did not alter the vortices. In the case of vortex core radius, however, the shape of that trend is not so simply explained. This trend shows a decrease in core radius as the rotor speed is increased from 60 rpm to roughly 250 rpm. After that, the radius increases with the rotor speed out to the highest speed, 600 rpm. Two primary phenomena are in conflict here, one which causes the radius to decrease and one which causes the radius to increase.

Increased circulation on the blade (at increased speeds) causes an increase in both the viscous and inertial forces acting on the vortices. The inertial forces act to move the peak swirl velocity closer to the vortex center, reducing the core radius. The viscous forces cause diffusion, which moves the peak velocity away from the center and increases the core radius.

Two parameters can be used to estimate the boundary between these regimes:

$$\text{the vortex Richardson Number:} \qquad R_{i_v} = \frac{\frac{2V_\theta}{r^2}\frac{\partial}{\partial r}(V_\theta\, r)}{\left(r\frac{\partial}{\partial r}\frac{V_\theta}{r}\right)^2}$$

$$\text{and the vortex Reynolds Number:} \qquad R_{e_v} = \frac{\rho V_{\theta\,\max} R_c}{\mu} = \frac{\Gamma_v}{\nu}$$

For the Lamb-Oseen vortex profile, the local vortex Richardson number, R_{i_v}, is a function only of the normalized distance from the vortex center, $\bar{r} = \frac{r}{R_c}$, and not of other vortex characteristics such as Γ_v. Figure 3.14 shows the vortex Richardson number for a Lamb-Oseen vortex plotted versus $\bar{r}$. The Richardson number is high in the vortex center and decreases with radial distance from the center. Since R_{i_v} decreases as $\bar{r}$ increases, it follows that the vortex core is more stable closer to the center. Figure 3.15 shows the vortex Reynolds numbers for each case tested here, which correlates nearly linearly with rotor rotation rate.

These two quantities determine the transition radius for each vortex inside of which the core is laminar, and outside of which the core is turbulent. It has been shown empirically in previous works [30] that vortex instabilities form in the region

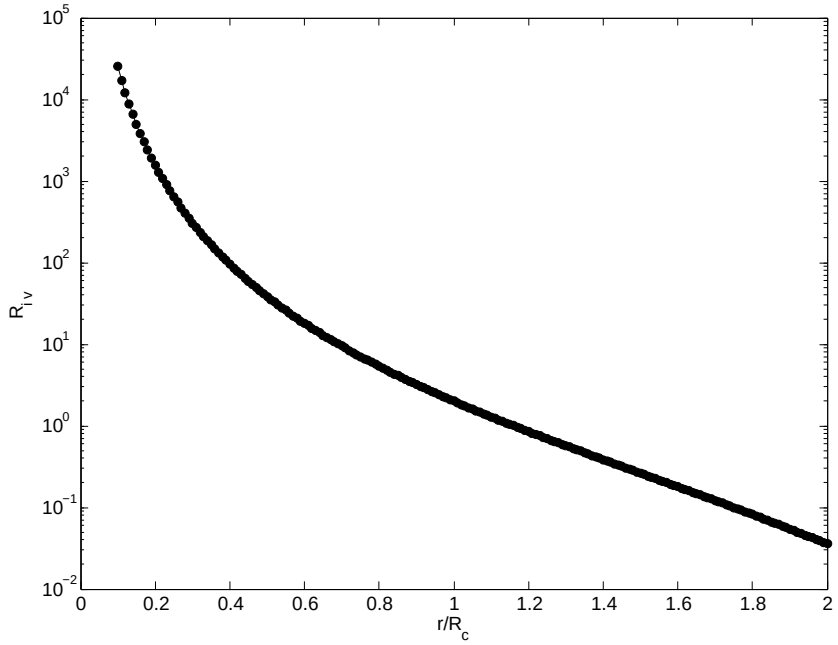

Figure 3.14: Vortex Richardson number

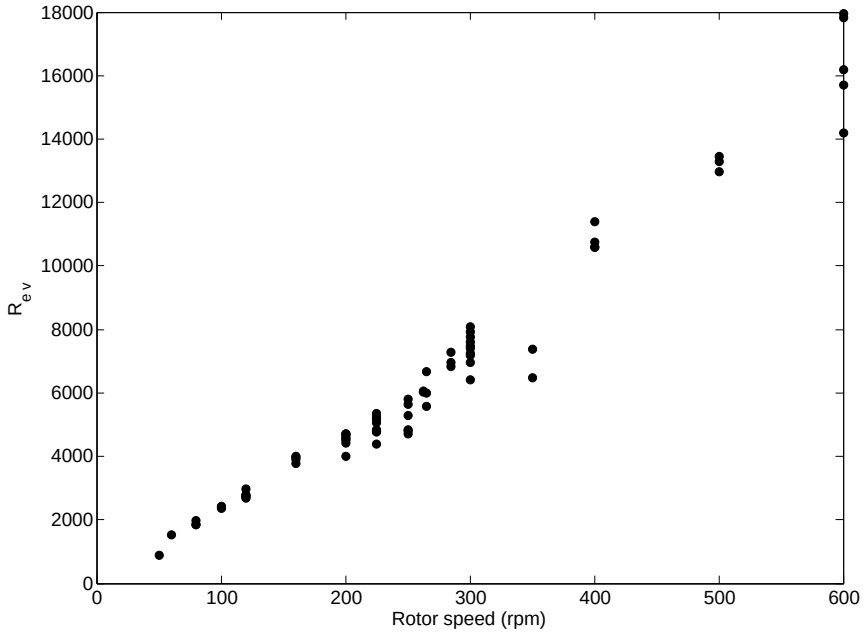

Figure 3.15: Vortex Reynolds number

where:

$$R_L = {}^{R_{i_v}}/_{R_{e_v}^{1/4}} < 1$$

R_L is called the relaminarization parameter. The laminar-turbulent transition radius, $\bar{r}^*$, is the solution of $R_L(\bar{r}) = 1$, and varies proportionally to $R_{e_v}^{-1/4}$. Depending on $\bar{r}^*$, a vortex may have more area in the laminar region than in the turbulent region or the other way around. Figure 3.16 shows the ratio of laminar core area to turbulent core area based on the average vortex circulation for each case tested. The transition occurs between rotor speeds of 200 and 300 rpm; this range also contains the local minimum in the trend of R_c with respect to rotor speed (Fig. 3.13). Analysis of the relaminarization parameter supports the idea that the range of cases tested here crosses from predominantly laminar to predominantly turbulent vortices, and that the effects of this on the vortex velocity profile can justify the nonlinear trend observed in the vortex core radius measurements.

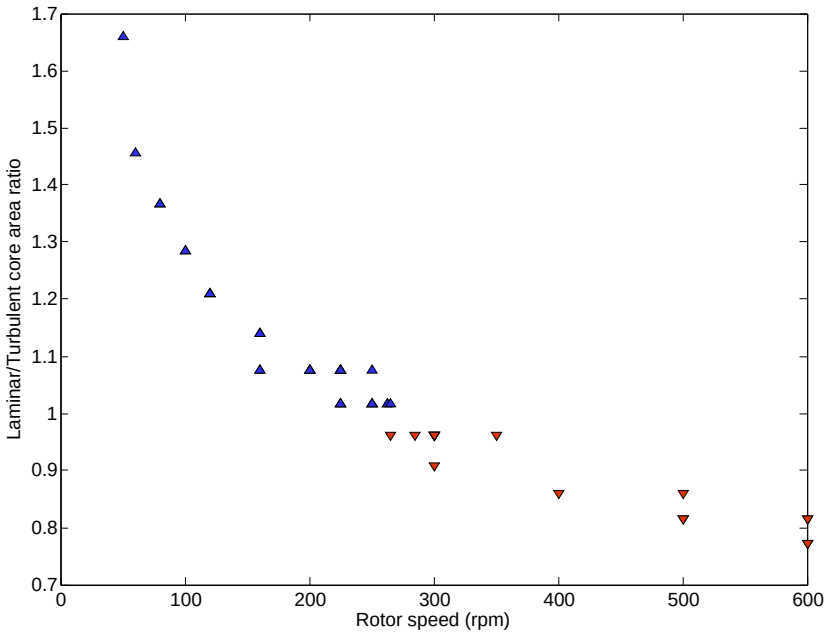

Figure 3.16: Ratio of laminar core area to turbulent core area as a function of rotor speed

3.1.2 Turbulent kinetic energy

In addition to the three vortex characteristics, the unsteady wake was analyzed in terms of its turbulent kinetic energy, k. The spatial distribution of k associated with all velocity fluctuations from the example 400 rpm, 50 µm steel sediment data set is shown in Fig. 3.17. The area of highest k corresponds to the location of the tip vortices as they enter the field of view.

The mean value of k was computed for each data set. This data is plotted versus rotor speed in Fig. 3.18. It is seen that k is proportional to the square of the rotor speed, and that the sediment presence has no significant affect on the turbulent kinetic energy measurements.

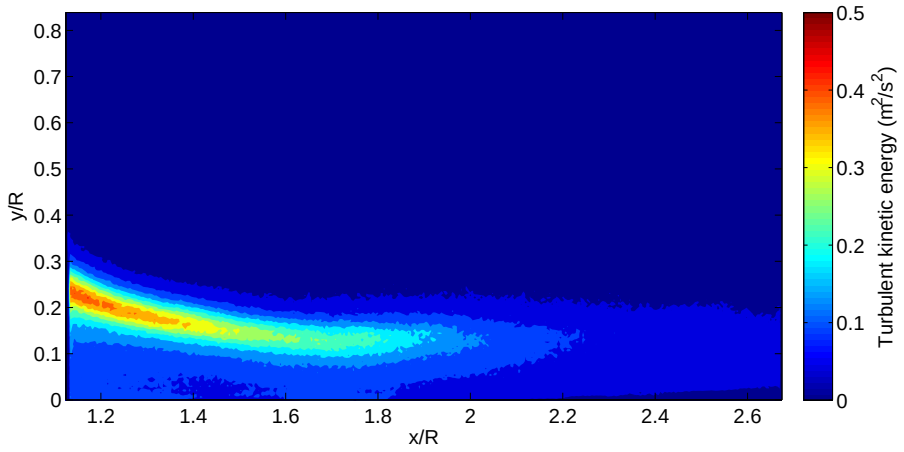

Figure 3.17: Turbulent kinetic energy distribution. 50 µm steel particles, 400 rpm.

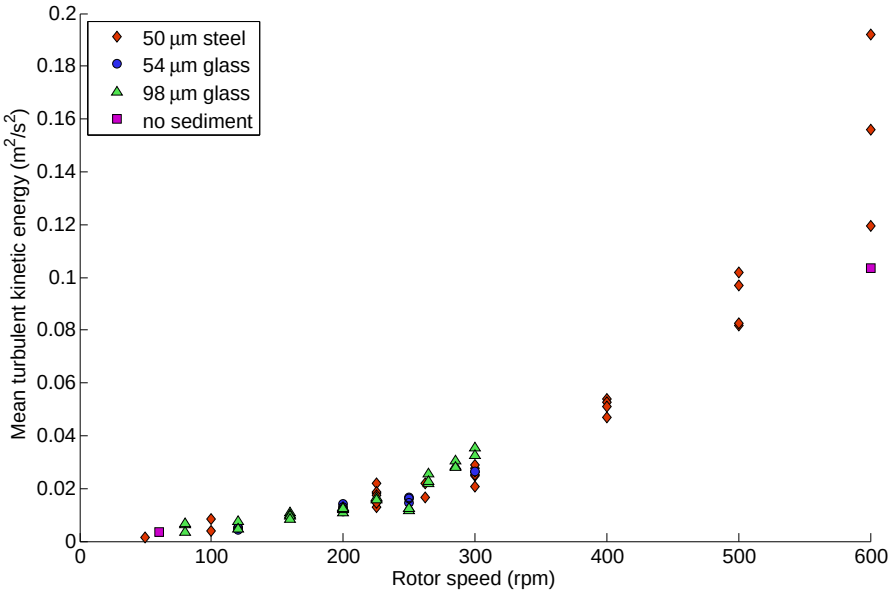

Figure 3.18: Turbulent kinetic energy measurements

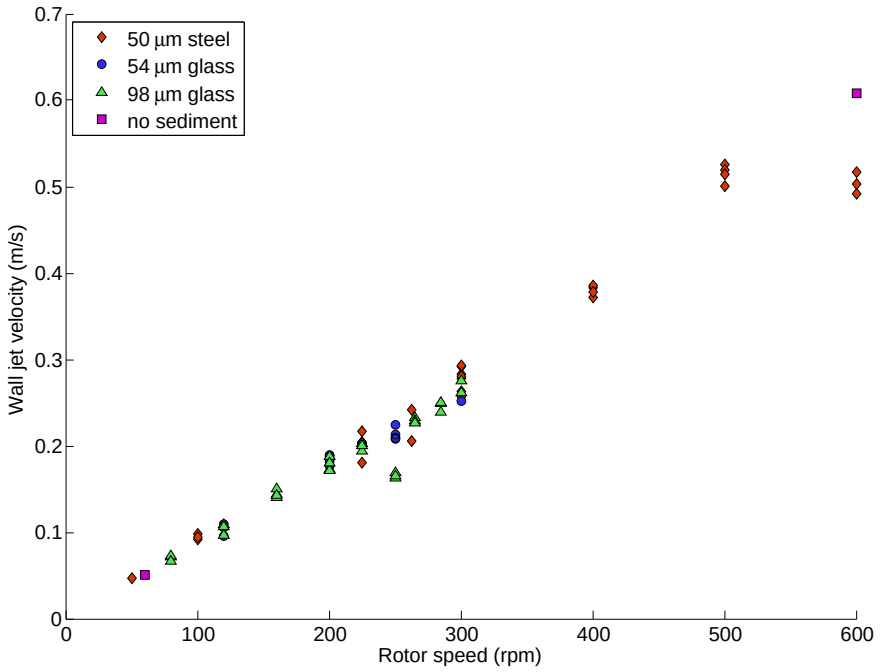

Figure 3.19: wall jet velocity measurements

3.1.3 Wall jet velocity

The dominant steady component of rotor-induced flow is the wall jet. The wall jet velocity was characterized using the time-averaged velocity field. The maximum horizontal velocity in the wall jet velocity profile was recorded as the characteristic wall jet velocity for the data set. Wall jet velocity versus rotor speed is plotted in Fig. 3.19. The wall jet velocity increases linearly with increasing rotor speed, and is not altered by the different sediment types.

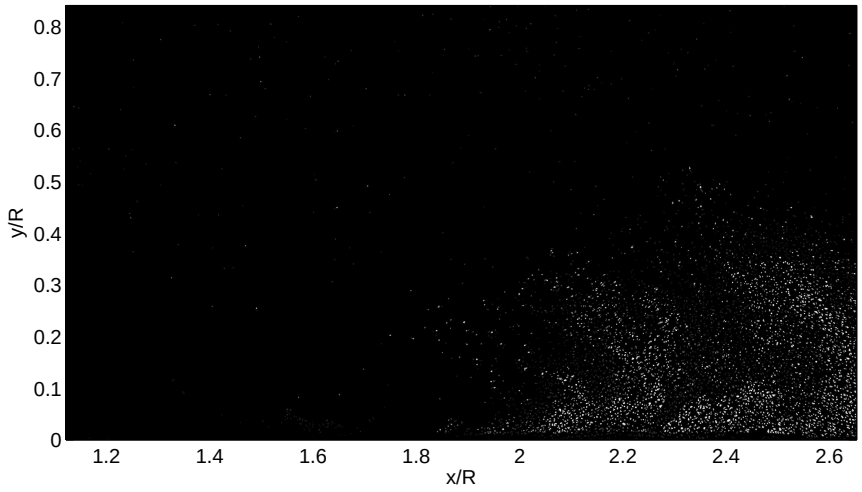

Figure 3.20: Dispersed phase particles identified from PIV image. 50 µm steel particles, 400 rpm.

3.2 Dispersed Phase

The dependent variable of this investigation is the quantified severity of sediment mobilization. This has been defined for this thesis as the mean number of sediment particles visible in each image of a data set. A filtered version of the previously shown Fig. 3.1 is given in Fig. 3.20. The median filter, Khalitov search function, and minimum threshold procedures described in chapter 2 are used here to isolate the dispersed phase in the two-phase image. This process identified 573 lifted sediment particles in this image.

Figure 3.21 shows the number of suspended sediment particles in the field of view over time for the same 400 rpm, 50 µm steel sediment example case. It is useful to look at the variance and frequency content of this data. If the sediment uplift was exclusively dependent on the passing of regularly spaced tip vortices, it would be

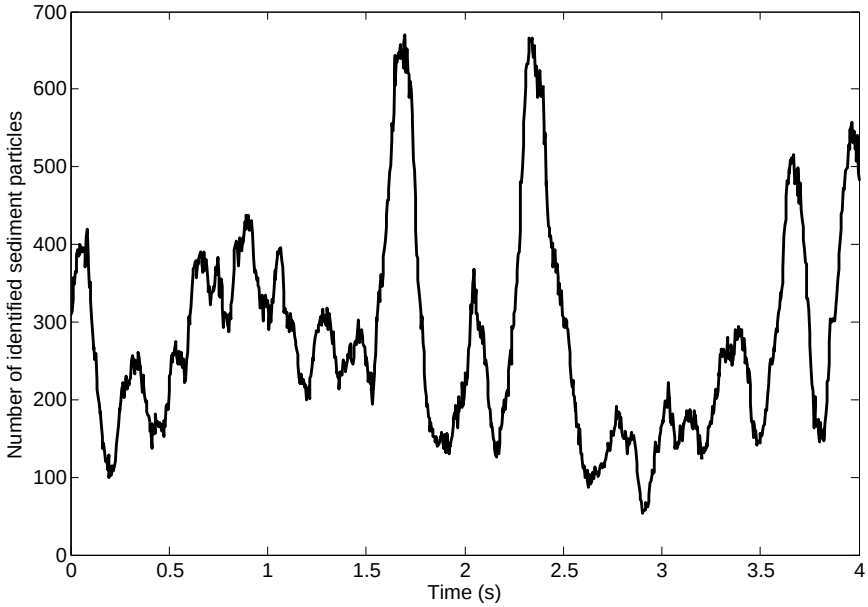

Figure 3.21: Instantaneous sediment measurement over time. 50 µm steel particles, 400 rpm.

expected that the sediment measured over time would display an oscillation at the blade passage frequency. Inspection of these measurements by frequency analysis shows that this oscillation is not significant. Figure 3.22 shows the Fourier frequency spectrum contained in the data of sediment mobilization over time for this same data set. There is not a significant peak at the vortex passage frequency, but there are peaks at two and four times that frequency. The frequency content indicates that the vortices are at least slightly aperiodic and that the sediment uplift is related also to the secondary events such as bombardment and vortex bundling.

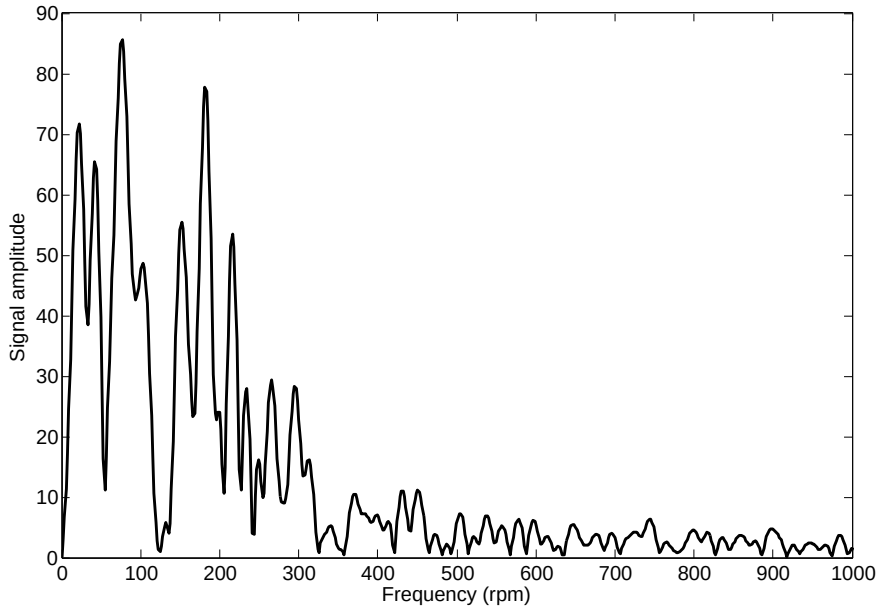

Figure 3.22: Frequency content of sediment measurement over time (rotor rotation rate 400 rpm)

The sediment quantification resulted in a sediment particle count for each image and a mean sediment count for each data set. The quantified sediment uplift is the mean number of particles present in each of the 2000 images which make up the data set. Thus the sediment mobilization resulting from the flow conditions present in each data set was characterized using a single scalar.

It is expected that this mean sediment uplift will be greater in a flow field of greater energy, and that the flow will have more energy in cases with a higher rotor speed. For each sediment type, it is therefore expected that the mean number of lifted particles will increase with increasing rotor speed. Figures 3.23–3.25 show sediment uplift plotted versus rotor speed for each sediment type. It is shown that

the number of lifted sediment particles increases super-linearly with increasing rotor speed, and that the 98 µm glass sediment experienced more mobilization than either of the other sediment types.

The bars around each data point indicate the magnitude of the variations in instantaneous sediment mobilization during the data collection. The bars enclose the 95% confidence interval for sediment measurements under those conditions, indicating the expected range for any instantaneous sediment measurement. This variation is quite large; on average, the 95% confidence interval for sediment measurements was around 52% of the mean measurement. The high variance in instantaneous measurements is another indicator that sediment uplift is tied to the aperiodic passage of blade tip vortices and to the irregular interactions between these vortices. Additionally, this variance could support the significance of rotor wake asymmetry, as discussed in chapter 2. Figure 3.21 shows peaks in instantaneous sediment mobilization at 1.6 s and 2.4 s, which could correspond to the discrete mobilization events highlighted by Sydney [24]. The duration of these events is small enough compared to the data collection duration that the mean sediment quantification can still be considered characteristic for each data set.

3.2.1 Sediment measurement calibration

The higher mobilization of the larger particles observed here is counter-intuitive; the larger particles were expected to mobilize less easily and settle more quickly. Further inspection of this result logically begins with verification of the measurements.

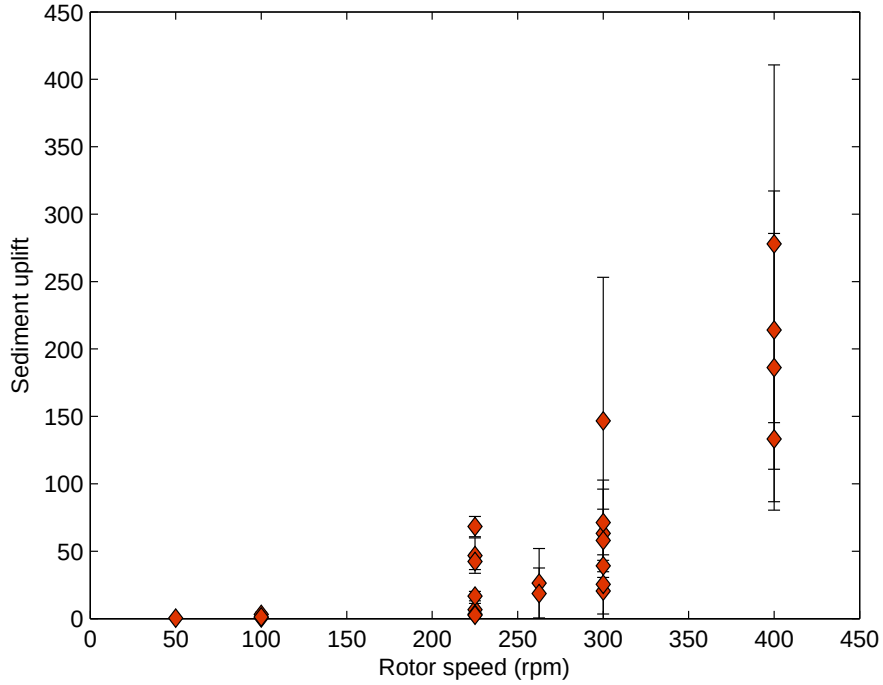

Figure 3.23: Mean sediment uplift versus rotor speed for 50 µm steel particles

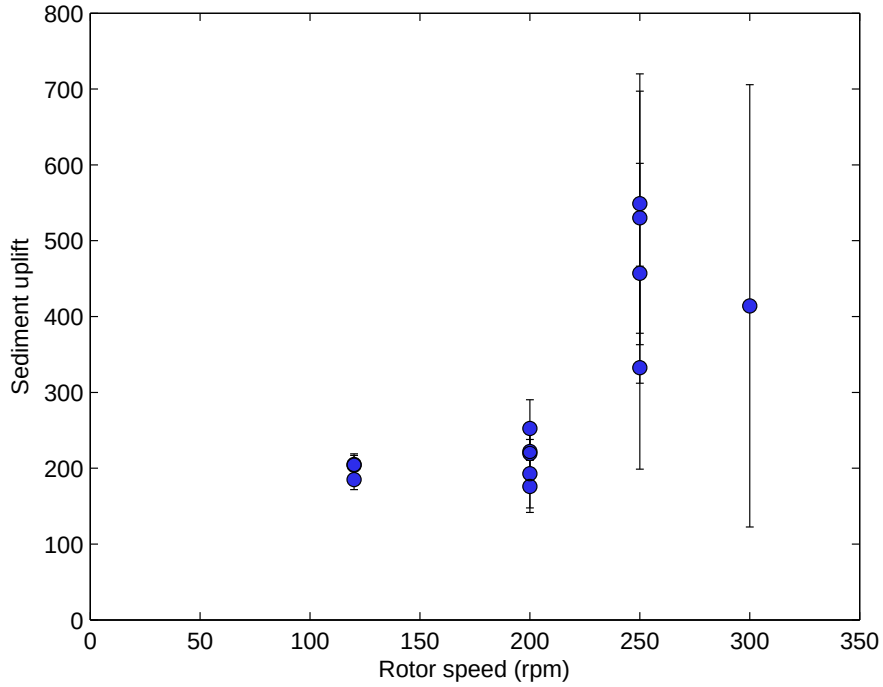

Figure 3.24: Mean sediment uplift versus rotor speed for 54 µm glass particles

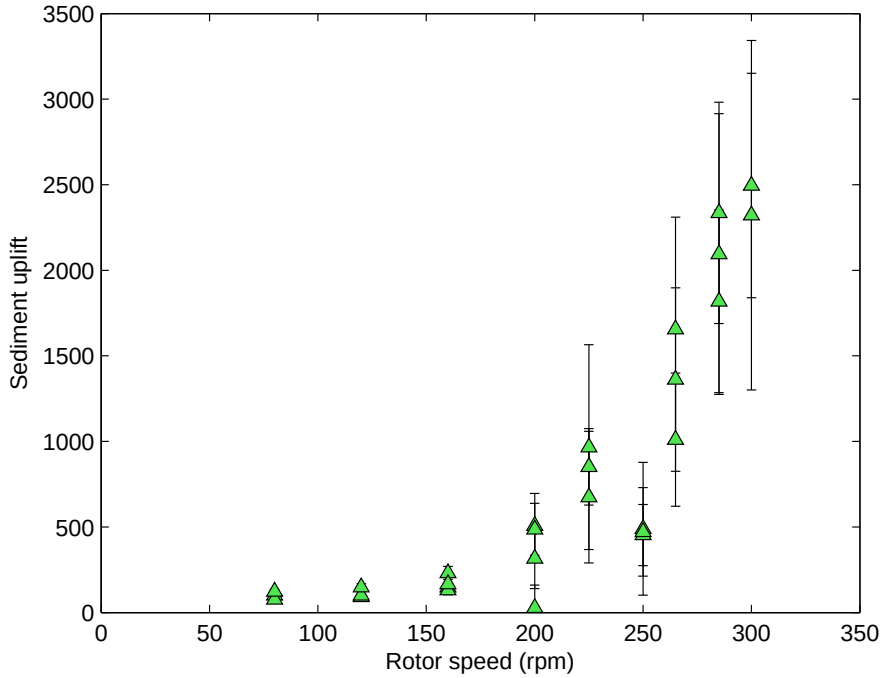

Figure 3.25: Mean sediment uplift versus rotor speed for 98 µm glass particles

As mentioned in chapter 2, the size and optical properties of the different sediment types could result in varied effective measurement volumes. This was addressed by changing the sediment identification criteria (see section 2.4.1) so that the identified number of particles was within 2% of the results of manually counting the visible sediment particles. Three images for each sediment type were tested this way. For manual identification to be practical, each of those images contained less than 300 visible, mobilized particles.

A previous work by Knowles and Kiger used a calibration procedure to identify the effective measurement depth for a particular sediment type [28]. Applying this procedure to each sediment type here can help to better understand the differences in measurement volume for each type. This calibration was performed by recording images of stationary sediment particles (suspended in alcohol gel, which has a simi-

lar index of refraction to water) at incrementally changing positions in the direction normal to the light sheet. In practice, this was accomplished by placing a sample of sediment particles mixed into hand sanitizer gel onto a computer controlled micrometer stage. The laser and optics were set up the same as in the primary data collection. The hardware and sample could not be placed underwater, so a smaller seeded water tank was placed in between the laser source and the sample to recreate the effects that PIV seed particles have on the laser sheet thickness. 10 images were recorded for each sediment type, and between each image the sample was shifted towards the camera by 200 µm. The laser sheet was roughly 3 mm thick, so some particles remained illuminated for the entire 1.8 mm traverse.

Applying the same sediment identification procedure described in section 2.4.1 to these samples gave the depths at which each type of sediment particle reflects enough light to be identified. The range of positions over which the particle is identified forms an effective measurement thickness, which will influence the measured quantity of mobilized sediment particles. For example, if the steel sediment was found to meet the threshold criteria at positions covering twice the depth in which the glass met the criteria, the measurements would indicate twice as much steel sediment as glass for the same actual concentration of particles in the flow.

Ideally, this procedure would be applied to the experimental setup exactly as it was used for the data collection. This was not possible here due to changes in the laser over time and due to the difficulty of adjusting the position of the sample under water. The setup was recreated as closely as possible, but the resulting sediment image values were found to be off by a constant factor. The procedure can still

be applied, but the images must first be normalized to the previous data. Instead of considering absolute brightness values recorded by the camera, the normalized procedure compares the recorded and threshold brightnesses relative to the recorded maximum brightness. For clarity, this can be shown as:

$$\text{normalized brightness} = \frac{\text{recorded brightness during calibration}}{\text{maximum brightness during calibration}}$$

$$\text{normalized threshold} = \frac{\text{threshold brightness for experiment}}{\text{maximum brightness during experiment}}$$

Figure 3.26 shows the normalized average brightness of pixels in each particle image compared to the particle's position in the light sheet (the normalized brightness threshold is indicated by the horizontal lines in Fig. 3.26). The measurement depth is visible as the range of positions for which the average brightness meets the normalized threshold. The measurement depth was found to be 2.7 mm for 50 µm steel particles, 2.6 mm for 98 µm glass particles, and 3.3 mm for 54 µm glass particles. This indicates that the optical properties of the sediment introduced up to 10% error to the sediment concentration measurements. This error is not insignificant, but it is not so large that it changes the trends observed in the data.

3.2.2 Sediment mobilization expectations

Increased confidence in the sediment measurements then leads to further investigation of possible reasons for higher mobilization of larger particles. One hypothesis for the increased mobilization of larger particles involves the relation between

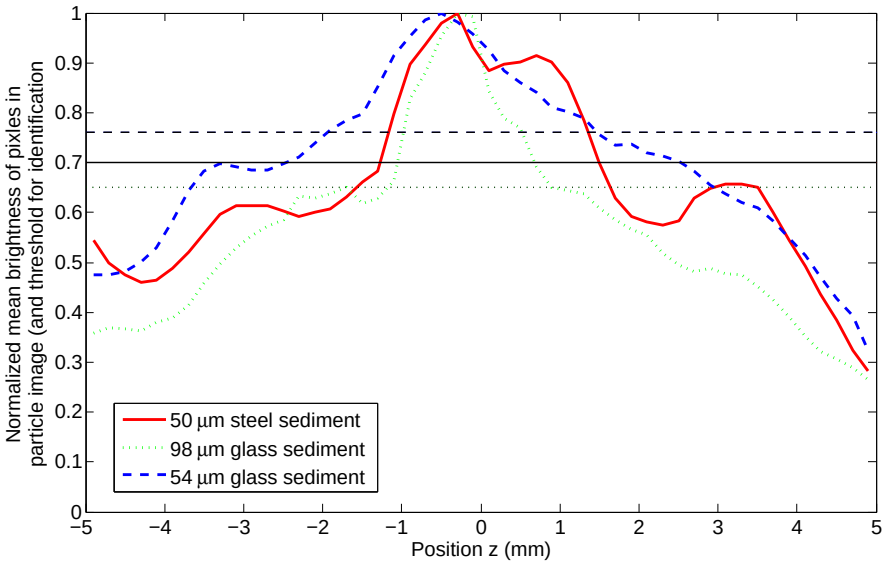

Figure 3.26: Measurement volume calibration by comparing particle image brightness to threshold brightness. Threshold values are represented by the horizontal lines.

each particle's diameter and the height of the laminar sublayer within the boundary layer over the sediment bed. If the larger particles reached significantly farther into the boundary layer than the smaller ones, the larger particles would experience greater fluid velocities and so perhaps mobilize more readily. The spatial measurement resolution of this experiment was not high enough to observe the boundary layer, but a rough estimate can be used to investigate this hypothesis.

Assuming the flow along the sediment bed to be a fully-developed turbulent boundary layer with no pressure gradient, the boundary layer height can be estimated from previous work as $\delta = 0.37 x Re_x^{-1/5}$ [31]. The necessary assumptions for this result are not quite true in the case of hover in ground effect (there is certainly a non-zero pressure gradient), but this approximation can still provide an estimate of δ. Using the measured U_{wall} as the characteristic velocity and a range of x covering

the field of view, it was found that $\delta \geq 4\,\text{mm}$ for all cases in this thesis (δ grows as the flow moves radially outward and increases with increasing U_{wall}). This height is comparable to the boundary layer estimate provided by previous related work [7]. The laminar sublayer of a turbulent boundary layer extends to $y \approx 0.1\delta = 400\,\mu\text{m}$. This indicates that all sediment types studied here are small enough to reside in the laminar sublayer. Since this does not separate the large and small particles, this hypothesis is not likely to explain the higher mobilization of the larger particles.

Alternately, the higher mobilization of larger particles could occur due to particle cohesion, which is greater for smaller particles. While particle cohesion is not accounted for by the Bagnold model of threshold friction velocity used in this thesis [8], the model by Greeley and Iverson and the model by Shao suggest that particle cohesion is an important factor in the threshold friction velocity of small spheres [18, 20]. However, those models were developed in air, and this research takes place in water. Since cohesion is very sensitive to the materials of the particles and fluid, it is likely that the cohesion experienced in this work is different than that predicted by either model. However, if the trends of these models for particles in air still hold for particles in water, the results of this thesis could be explained by particle cohesion. The cited models are compared in figure 3.27.

Even without being certain of the magnitude of the cohesive forces involved, the relationship between bombardment and cohesion could lead to higher mobilization of the larger glass particles compared to the smaller ones observed in this work. As particle diameter decreases (for a given velocity and density), a particle's momentum decreases and the particle's resistance to mobilization, U_{*_t}, due to cohe-

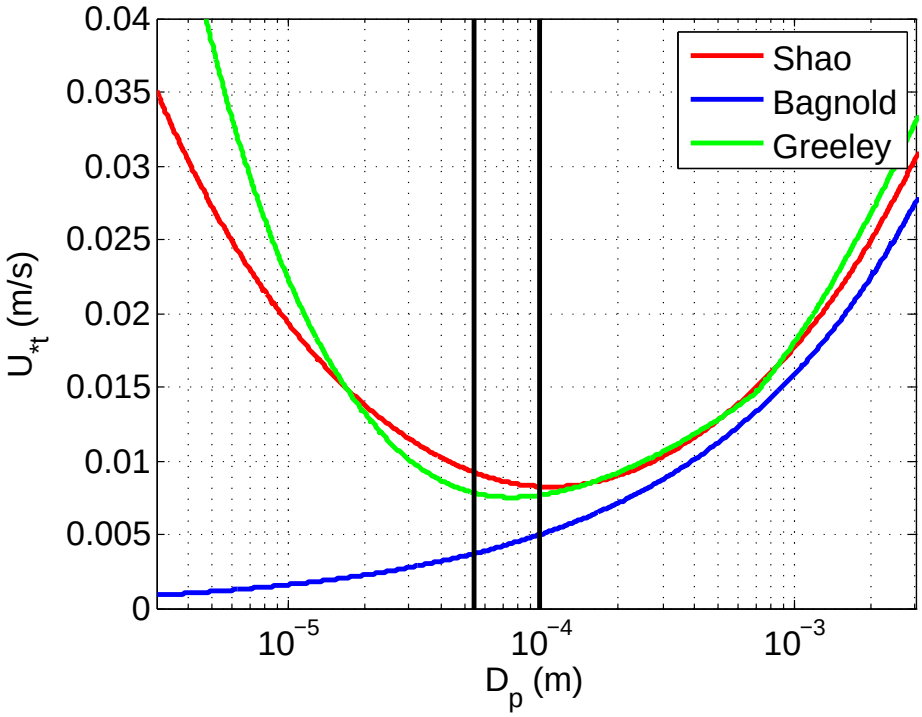

Figure 3.27: Threshold friction velocity models for glass in water. 54 µm and 98 µm are highlighted in black.

sion increases. In practice, this effect would make bombardment less effective as a mechanism of mobilizing additional sediment since the impact of a particle into the sediment bed is less able to overcome the cohesive forces and free other particles. The larger particles experience less cohesion and have higher momentum, and so are moved more readily by bombardment. This interaction is especially significant for particle sizes near or below the minimum U_{*_t} which occurs near $D_p = 100\,\mu\text{m}$. In this region, U_{*_t} increases due to cohesion as D_p decreases. Above this region, U_{*_t} increases due to weight as D_p increases. The sediment particles selected for this work have coincidentally fallen near the minimum U_{*_t} (the two sizes of glass particles are highlighted by the black lines in figure 3.27). Because of the specific particle sizes, the influence of cohesion in this experiment is thought to be relatively high. This influence alters the effects of bombardment and leads to the unexpected result of highest mobilization for the largest sediment type.

3.3 Scaling Parameters

At this point, each test of each flow condition has been assigned a single value of sediment uplift and a set of values for flow characteristics. The parameters which varied between cases tested in this thesis are listed in table 3.1. The goal of this thesis is to identify a group of the measured flow characteristics that can be used to relate and predict sediment mobilization. To accomplish this, the flow

characteristics must be grouped and inspected for meaningful correlation with the measured sediment mobilization. Each of the following plots will compare sediment uplift to a parameter group.

Table 3.1: Rotor-induced sediment mobilization system characteristics studied for candidate scaling parameters

Parameter	Symbol	Units
Sediment diameter	D_p	m
Sediment density	ρ_p	$\mathrm{kg\,m^{-3}}$
Sediment terminal velocity	U_F	$\mathrm{ms^{-1}}$
Sediment threshold friction velocity	U_{*t}	$\mathrm{ms^{-1}}$
Wall jet velocity	U_{wall}	$\mathrm{ms^{-1}}$
Vortex circulation	Γ_v	$\mathrm{m^2s}$
Vortex core radius	R_c	m
Vortex peak swirl velocity	$V_{\theta\,\mathrm{max}}$	$\mathrm{ms^{-1}}$
Turbulent kinetic energy	k	$\mathrm{m^2s^{-2}}$

3.3.1 Existing scaling parameters

Previous work used Buckingham-Π dimensional analysis to group the rotor-induced sediment mobilization system characteristics into candidate scaling parameters. Many dimensionless parameter groups were identified, and 5 were proposed

as likely scaling parameters [19]. These 5 parameters are:

$\frac{\Gamma_v}{D_p U_{*_t}}$ called the stationary inertia ratio

$\frac{\Gamma_v}{D_p U_F}$ called the mobile inertia ratio

$\frac{V_{\theta\,\max}}{U_F}$ called the terminal-swirl velocity ratio

$\frac{V_{\theta\,\max}}{U_{*_t}}$ called the threshold-swirl velocity ratio

$\frac{V^2_{\theta\,\max}}{U_F U_{*_t}}$ called the terminal/threshold-swirl velocity ratio

The data recorded for that study did not span enough of the scaling parameter axis to assess the correlation with sediment mobilization. The results were therefore inconclusive. The data from this study spans more of the parameter axis, enabling a re-evaluation of these candidate scaling parameters. Plots of sediment uplift versus each of these parameters are shown in figures 3.28–3.32. It is visible from these that some correlation exists for each sediment type, but that these parameters do not collapse the trends of all different sediment types. It is important to note that although the largest particles in this study experienced the greatest mobilization this trend is not expected to continue for significantly larger particles (see section 3.2.2).

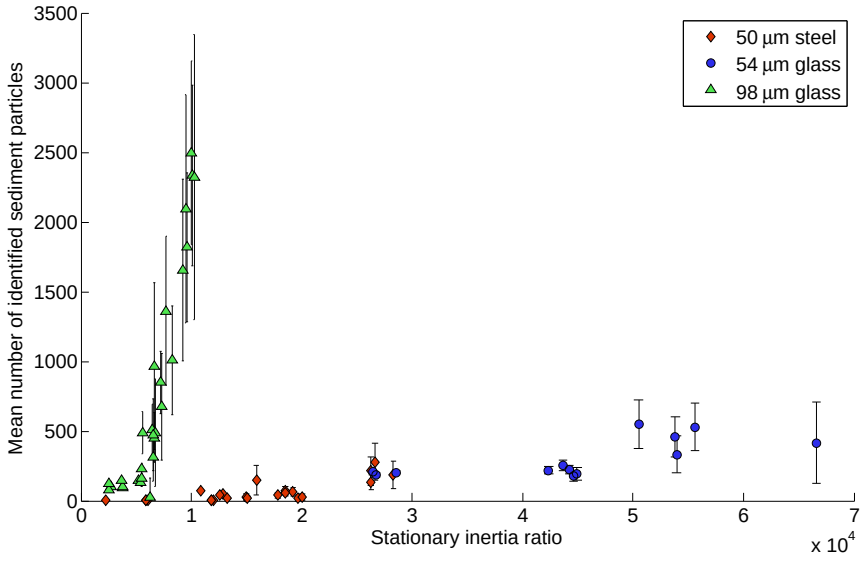

Figure 3.28: Stationary inertia ratio

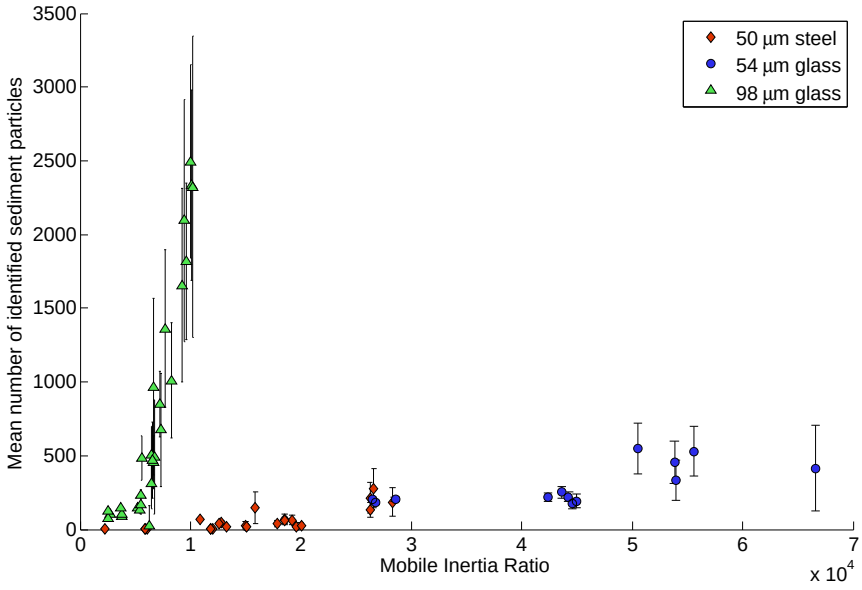

Figure 3.29: Mobile inertia ratio

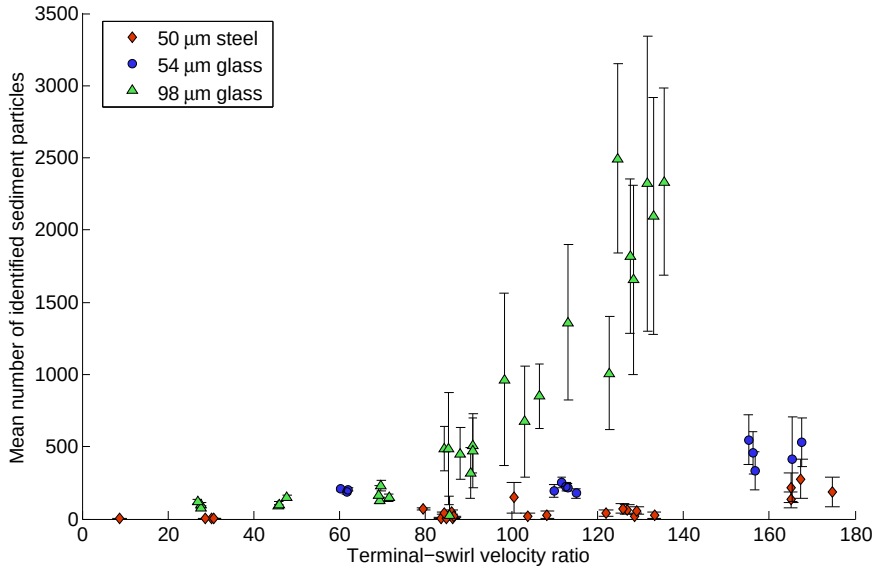

Figure 3.30: Terminal-swirl velocity ratio

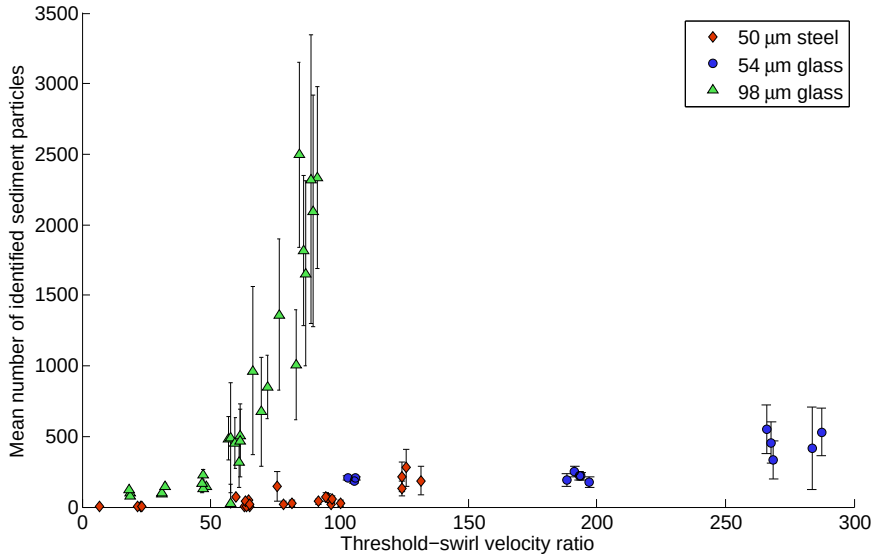

Figure 3.31: Threshold-swirl velocity ratio

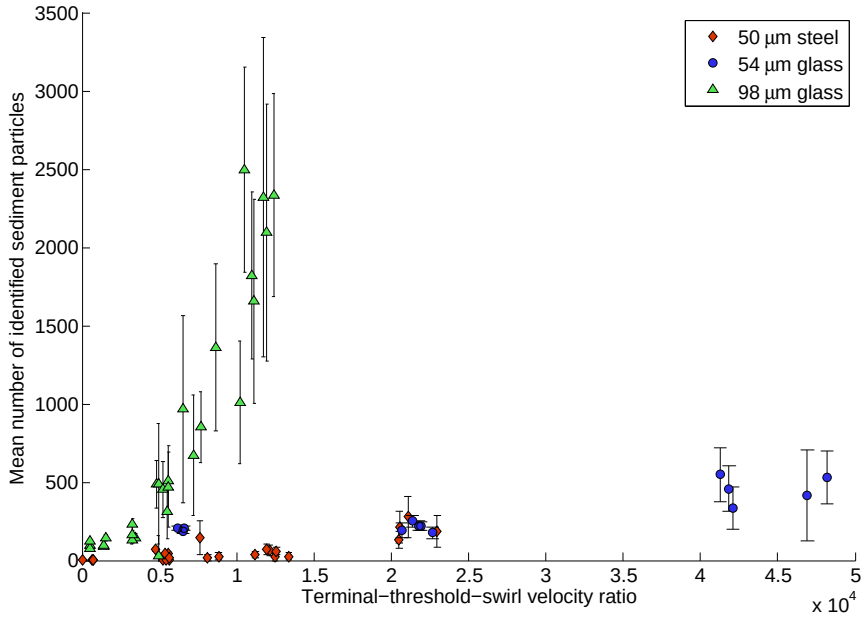

Figure 3.32: Terminal/threshold-swirl velocity ratio

3.3.2 New parameter groups

To identify parameter groups which correlate with data for all sediment types, the search was widened to parameter groups with remaining dimensions. These parameter groups do not meet the standard definition of a scaling parameter, but are no less likely to correspond to a meaningful correlation between system characteristics and sediment mobilization.

Because there are so many system parameters to inspect, and because these parameters could carry one of many exponents (squared, cubed, square root, or first power, for example), the permutations and combinations of these are too numerous to thoroughly search. For example, inspecting the 9 varied parameters measured here and allowing each to appear under exponents of ± 1, ± 2, or $\pm 1/2$ results in

over 1.8×10^{16} possible combinations. This is found using binomial coefficients (the "n-choose-k" problem), which states that given n items from which to choose, there are $\frac{n!}{k!(n-k)!}$ possible combinations of k chosen items. To establish a practical limit on the number of combinations to search, it was chosen that the scaling parameters to be inspected would be a combination of no more than 5 of the individual measured parameters (including variations in exponent). With this restriction, there are 3,505,050 possible combinations to inspect. On a basic workstation computer, this processing completed in roughly 40 hours.

3.3.3 Correlation detection

The analysis of each parameter group was carried out by inspecting a curve fit to the data of sediment uplift. The curve which was fit to each scatter plot was a scaled power curve, $y = a \times x^b$. Both constants a and b were limited to be positive. This curve fits linear and super-linear trends, is monotonic, and predicts zero sediment uplift in the case of zero flow. Each of these characteristics makes this function ideal for quickly searching for correlations. Figure 3.33 shows an example of this curve fit. For each parameter group, the constants a and b were determined using least squares regression to find the best curve fit to all of the measured data.

Once the parameter groups are created, the next task is to automatically analyze their correlation with sediment uplift. To identify the best of the parameters, this analysis requires more than a goodness-of-fit statistic. However, the R^2 goodness-of-fit statistic is still a useful first look at the correlation. Only parameter

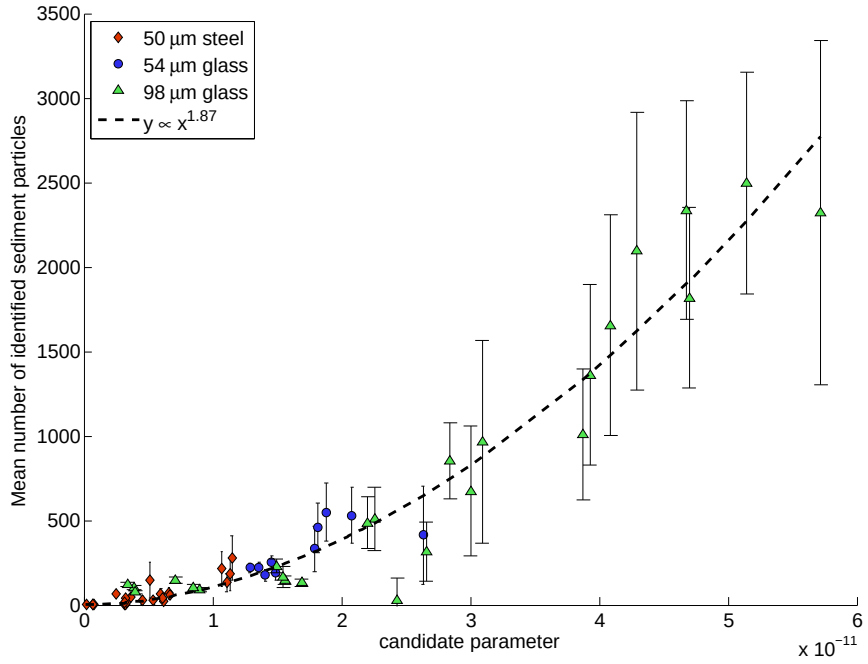

Figure 3.33: $y = a \times x^b$ fit to scatter of scaling parameter and sediment uplift

groups for which $R^2 \geq 0.9$ were considered further. This indicates that the mean residuals of the curve fit (the separation between each data point and the values predicted by the curve) for each of these parameters was at most 10% of the variance of that data.

It is notable that some parameters with high R^2 values did not necessarily fit the data well. A curve may fit the scatter of all data points well, but when compared to a logical subset of the data (for instance, consider only the data recorded using steel sediment) the model and measurements diverge. The inability to test for this is a weakness of an R^2 test which must be overcome in order to better assess candidate parameter groups. Figure 3.34 shows an example curve fit for which the high R^2 value is misleading. To address this, each trend for which the R^2 value considering all

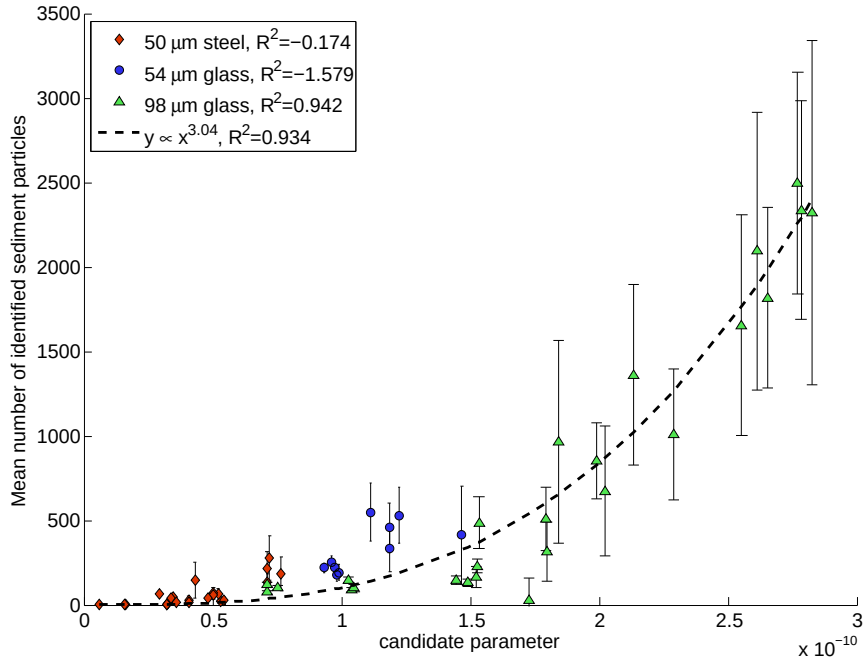

Figure 3.34: Curve fits full data set well, but fits very poorly to data from 54 µm glass and 50 µm steel sediment

data is sufficiently high is then broken apart into three sets of data, each containing measurements made using only a single sediment type. The same curve is then tested for a new R^2 value using only this subset of the data. Only trends for which all subsets returned $R^2 \geq 0.5$ were considered further.

3.4 Proposed Scaling Parameters

After these eliminations, three candidate scaling parameters stood out. These are each presented here, along with a discussion of physical interpretation, similar alternative parameter groups, and normalization by characteristic scales.

3.4.1 Parameter $\mathbb{A}$

The first parameter group which passed the criteria described above is:

$$\mathbb{A} = \frac{D_p^{2.5} V_{\theta\,\max}^2}{U_{*t}^3}$$

The plot of rotor-induced sediment mobilization versus parameter $\mathbb{A}$ is shown in Fig. 3.35. The parameters and exponents included in this group indicate that sediment uplift increases for particles of larger diameter, sediment uplift decreases for particles of higher threshold friction velocity, and sediment uplift increases for conditions of higher vortex peak swirl velocity. Each of these individual trends agrees with the previously displayed results. Remember, however, that the increased mobilization for larger particles (discussed in section 3.2.2) is not expected to continue far outside of the parameter space measured here.

Parameter $\mathbb{A}$ is related to the previously proposed threshold-swirl velocity ratio.

$$\mathbb{A} = \frac{D_p^{2.5}}{U_{*t}} \left(\frac{V_{\theta\,\max}}{U_{*t}} \right)^2$$

This threshold-swirl velocity ratio is here scaled by $\frac{D_p^{2.5}}{U_{*t}}$, a set of sediment characteristics which collapses data for different sediment types to a single correlation.

The curve fit indicates that the sediment uplift correlates with this parameter group by the relation $y = (1.06 \times 10^{10}) \times x^{1.92}$. The R^2 value for this correlation was high for the overall data, the 98 µm glass particle data, and the 50 µm steel particle

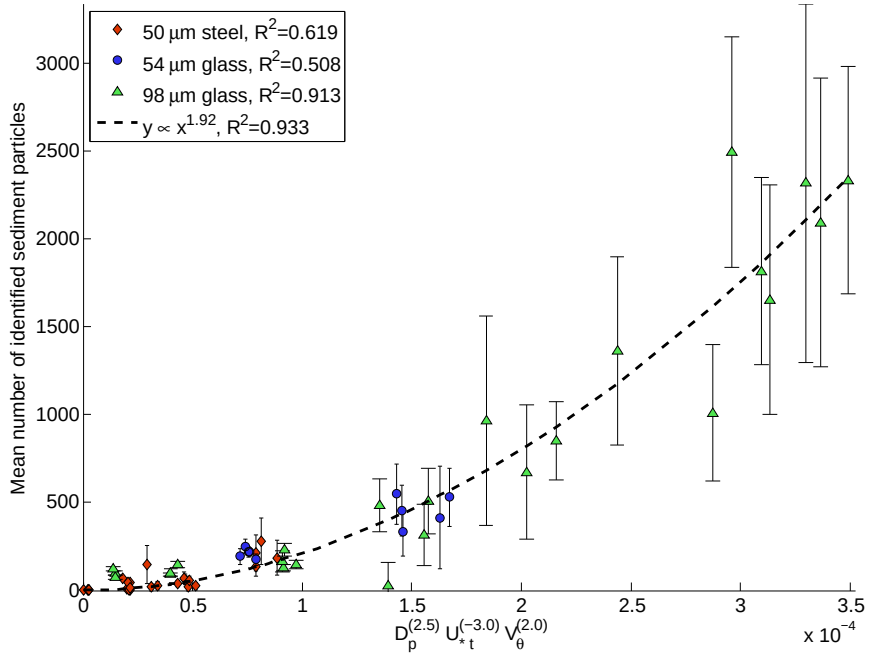

Figure 3.35: Rotor-induced sediment mobilization plotted against proposed scaling parameter $\mathbb{A}$

data, but lower for the 54 µm glass particle data. The 54 µm glass particle data fits least well in nearly every identified parameter group; this can be attributed to the minimal range across the x-axis which this subset of the data spans.

A potentially useful alternative parameter group is:

$$\mathbb{A}' = \frac{D_p V_{\theta\,\max}^2}{\rho_p^{1.5}}$$

This parameter replaces U_{*_t} with $(\rho_p D_p)^{0.5}$. This switch is reasonable because threshold friction velocity is related to the sediment diameter and density, but it is not a perfect replacement since the relationship is complicated and non-linear. This related parameter group is simpler to measure because it does not require knowledge

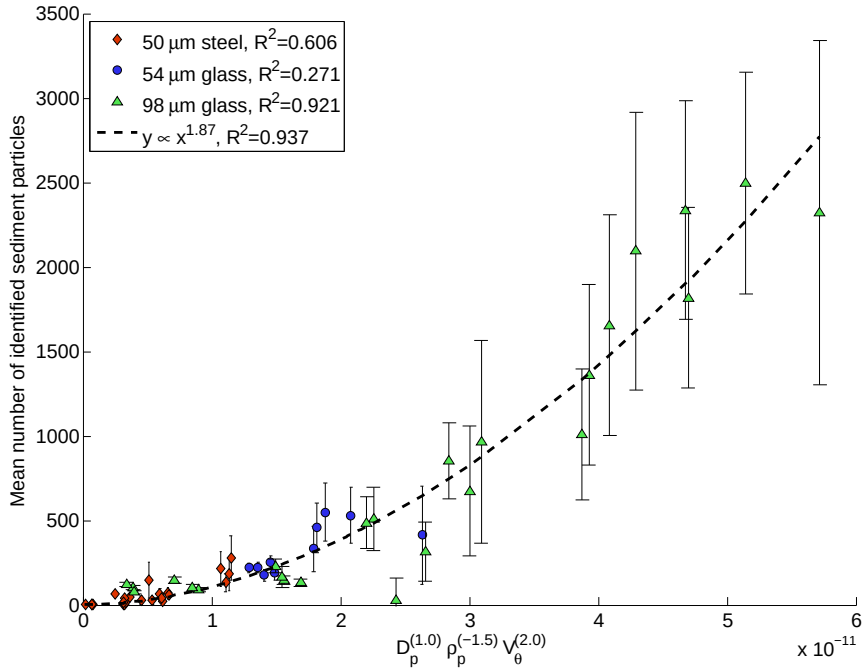

Figure 3.36: Similar parameter group to $\mathbb{A}$

of the actual sediment threshold friction velocity, but it is potentially less accurate, especially for extrapolation. In the range of data measured in this thesis, there does not seem to be a significant difference between these parameter groups. This parameter is plotted in Fig. 3.36. The best fit is defined by $y = (3.94 \times 10^{22}) \times x^{1.87}$.

3.4.2 Parameter $\mathbb{B}$

The second parameter group identified is:

$$\mathbb{B} = \frac{D_p^{0.5} U_{\text{wall}}^{1.5}}{\rho_p R_c}$$

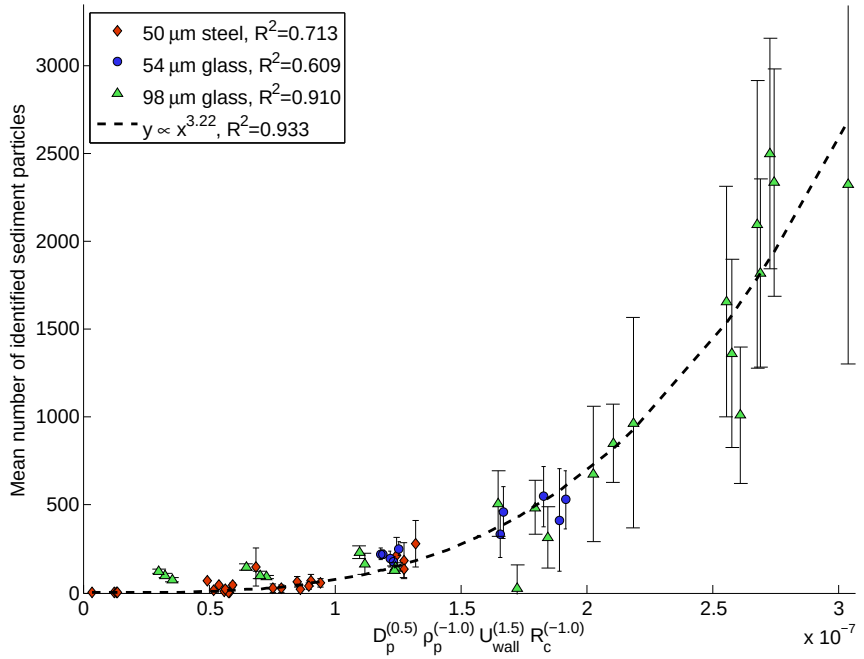

Figure 3.37: Rotor-induced sediment mobilization plotted against proposed scaling parameter $\mathbb{B}$

The plot of rotor-induced sediment mobilization compared to this parameter is shown in Fig. 3.37. The correlation for this parameter is defined by $y = (2.76 \times 10^{24}) \times x^{3.22}$. As with parameter $\mathbb{A}$, this shows that sediment uplift increases for particles of larger diameter. Additionally, sediment uplift decreases for particles of higher density, sediment uplift increases for conditions of higher wall jet velocity, and sediment uplift decreases for conditions of higher vortex core radius. The connections to sediment density and wall jet velocity agree with previous results, but the connection to vortex core radius is less clear.

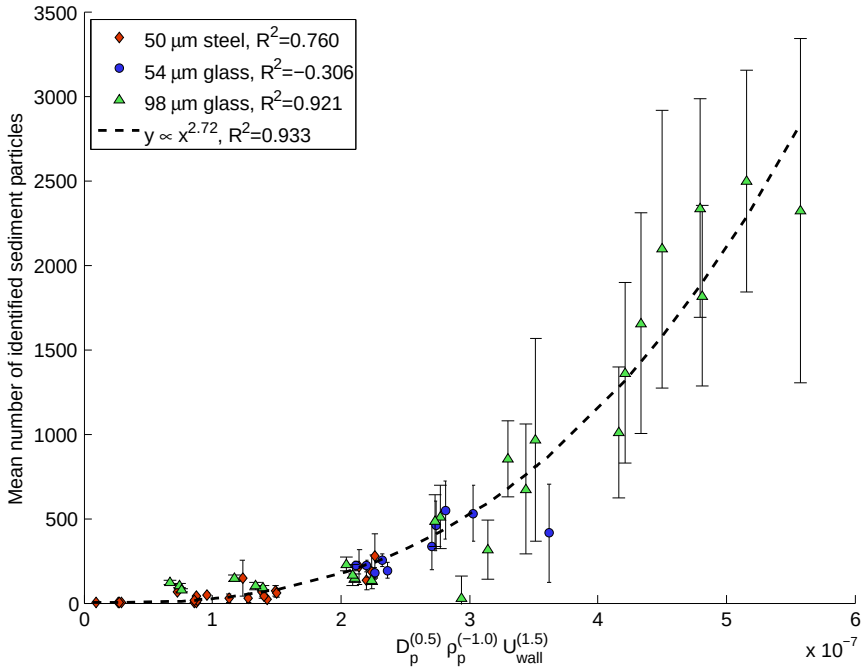

Figure 3.38: Scaling parameter $\mathbb{B}$ with vortex core radius removed

Vortex core radius alone does not correlate with sediment uplift. Because of this, the inclusion of vortex core radius in the parameter group is suspect. To inspect the contribution of vortex core radius to parameter $\mathbb{B}$, Fig. 3.38 shows the data plotted for the parameter with vortex core radius removed. The altered correlation is defined by $y = (3.10 \times 10^{20}) \times x^{2.72}$.

The result of removing R_c from this parameter group is difficult to interpret. The R^2 value for the whole data set remains unchanged. The R^2 values for 50 µm steel sediment and 98 µm glass sediment improve slightly. The R^2 value for 54 µm glass sediment decreases severely, so much that it becomes negative. This poor fit indicates that the modified parameter group does not correlate well with the results. As mentioned previously however, the data for 54 µm glass sediment nearly

always displays a low R^2 value as a result of the narrow span it covers along the x-axis. It is possible that this modification to parameter $\mathbb{B}$ is a superior predictor of sediment mobilization, although this is not statistically indicated in these plots. Unfortunately, this hypothesis cannot be adequately tested using the data available in this thesis.

3.4.3 Parameter $\mathbb{C}$

The third parameter group identified takes advantage of both the vortex measurements and the turbulent kinetic energy analysis. This parameter is:

$$\mathbb{C} = \frac{D_p^{0.5}\Gamma_v^{0.5}k^{0.5}}{\rho_p R_c^2}$$

Figure 3.39 shows this correlation. Because $\Gamma_v \propto V_{\theta\,\max} R_c$, this parameter can also be written

$$\mathbb{C} = \frac{D_p^{0.5}V_{\theta\,\max}^{0.5}k^{0.5}}{\rho_p R_c^{1.5}}$$

In addition to the previous trends, this parameter shows that sediment uplift increases for conditions of higher vortex circulation and for conditions of higher turbulent kinetic energy. The curve fit for this parameter is defined by $y = (2.64 \times 10^{13}) \times x^{2.58}$.

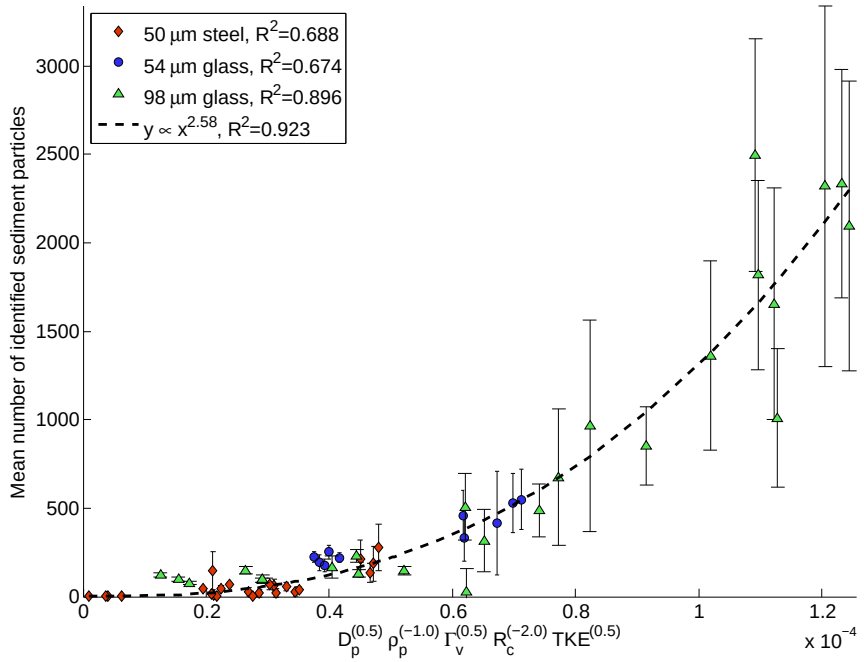

Figure 3.39: Rotor-induced sediment mobilization plotted against proposed scaling parameter $\mathbb{C}$

3.4.4 Dimensionless parameters

It is customary for scaling parameters to be dimensionless, i.e., combinations of individual system characteristics which are independent of scale and units. For example, boundary layer transition in flow over a plate occurs at the same Reynolds number regardless of the plate's size or the fluid properties. The plate's size is not unimportant to the boundary layer flow; it is included in the dimensionless Reynolds number and so does not need to be addressed separately. It is desirable that scaling parameters for rotor-induced sediment mobilization have these same traits. Ideally, these parameters would correlate over variations in a larger parameter space (including fluid density and rotor design characteristics), but the data in

this thesis cannot test that correlation. Creating scaling parameters that correlate with sediment mobilization for all cases requires the incorporation of many system parameters. This does not leave independent system parameters which could be used to normalize the scaling parameter, and so makes normalization very difficult.

For example, the admittedly unintuitive units of parameter $\mathbb{A}$ are $\mathrm{m}^{1.5}\,\mathrm{s}$. This parameter could be rendered dimensionless by multiplying it by a characteristic velocity and dividing it by a characteristic length to the power of 2.5, for example, the rotor blade tip speed, V_{tip} and the rotor radius, R.

$$\mathbb{A}^* = \frac{D_p^{2.5} V_{\theta\,\mathrm{max}}^2 V_{\mathrm{tip}}}{U_{*_t}^3 R^{2.5}}$$

However, normalization by these parameters would change the correlation exhibited by the dimensioned parameter because there is no independent characteristic velocity to normalize by. Multiplying by any available velocity measurement will change the placement of data on the parameter $\mathbb{A}$ axis. To demonstrate this, a normalized variation of parameter $\mathbb{A}$ is plotted in Fig. 3.40. It is apparent (especially by inspecting the R^2 value for steel sediment) that the parameter's correlation for data of each sediment type has been lost.

Parameters $\mathbb{B}$ and $\mathbb{C}$ are subject to the same difficulty. The units of parameter $\mathbb{B}$ are $\mathrm{m}^4\,\mathrm{s}^{-1.5}\,\mathrm{kg}^{-1}$. This parameter could be normalized by multiplying it by the fluid density and a characteristic length scale to the power 0.5 and dividing it by a characteristic velocity to the power 1.5. This normalization is problematic, as the typical characteristic velocity would be the wall jet velocity, which is included in

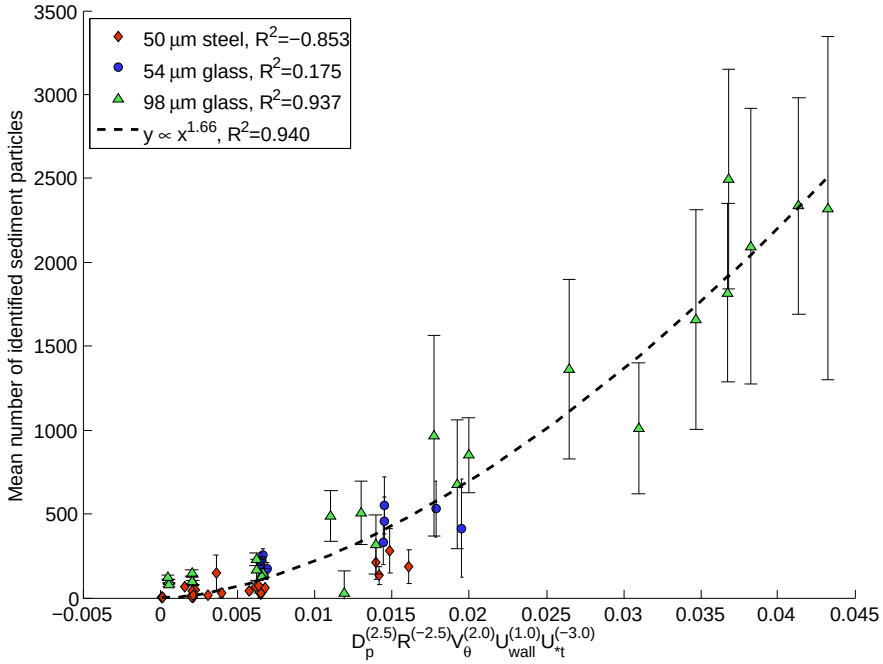

Figure 3.40: Dimensionless variation of parameter $\mathbb{A}$

the parameter group already. This could be normalized instead by a characteristic length scale and a characteristic time scale. In this case, the length scale is the rotor radius and the time scale is the blade tip passage period. This is effectively the same as normalizing by an alternate characteristic velocity, the rotor tip speed.

$$\mathbb{B}^* = \frac{D_p^{0.5} U_{\text{wall}}^{1.5} \rho R^{0.5}}{\rho_p R_c V_{\text{tip}}^{1.5}}$$

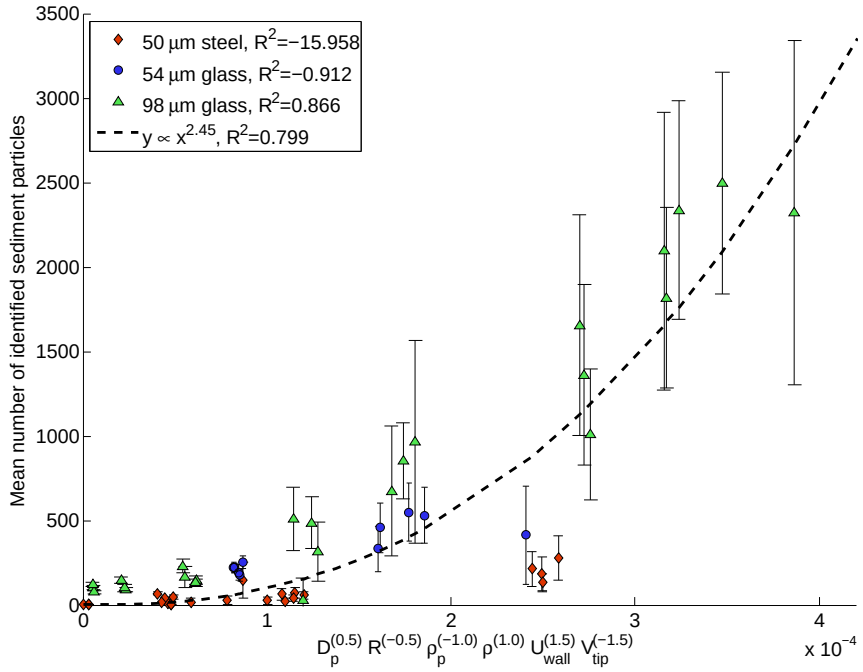

Figure 3.41: Dimensionless variation of parameter $\mathbb{B}$

The units of parameter $\mathbb{C}$ are $\mathrm{m}^{3.5}\,\mathrm{s}^{-1.5}\,\mathrm{kg}^{-1}$. This parameter could be normalized by multiplying it by the fluid density and a characteristic length scale and dividing it by a characteristic velocity to the power of 1.5.

$$\mathbb{C}^* = \frac{D_p^{0.5}\Gamma_v^{0.5}k^{0.5}\rho R}{\rho_p R_c^2 V_{\mathrm{tip}}^{1.5}}$$

Normalized parameters $\mathbb{B}$ and $\mathbb{C}$ are plotted in figures 3.41 and 3.42. Each shows divergence between cases of different sediment types.

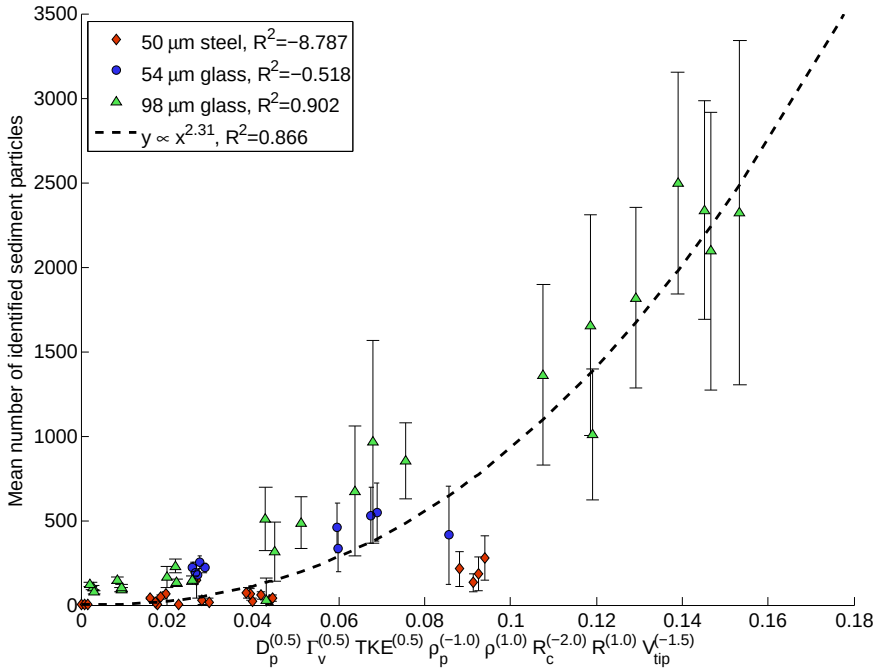

Figure 3.42: Dimensionless variation of parameter $\mathbb{C}$

3.4.5 Full-scale predictions

The new parameter groups display correlation versus sediment mobilization for all of the cases tested in this thesis. However, the laboratory and full scales are significantly different, requiring extrapolation to predict sediment mobilization at full scale from lab scale results. Extrapolation always introduces uncertainty, but in this case the uncertainty is greater because the lab scale results presented here do not vary the rotor radius or fluid density, which leaves the effects of those variations unknown (a full-scale helicopter in air varies in both of those parameters from the lab tests).

Table 3.2: Estimates of rotor-induced sediment mobilization parameter values for full-scale systems

Γ_v ($m^2\,s^{-1}$)	$V_{\theta max}$ ($m\,s^{-1}$)	R_c (m)	U_{wall} ($m\,s^{-1}$)	k ($m^2\,s^{-2}$)	Notes	From Ref.
37.53	37	0.21336			estimate	[19]
			20		estimated	[32]
9.3					low estimate	[3]
37.2					high estimate	[3]
	11.89	0.0214			low estimate	[33]
	41.45	0.0321			high estimate	[33]

D_p (µm)	ρ_p ($kg\,m^{-3}$)	U_F ($m\,s^{-1}$)	U_{*t} ($m\,s^{-1}$)		
200	2560	0.28	0.02	sand	[34]
1.49	2160		1.5	Kaolinite	[22]
3.549	2640		0.03	fine dust	[22]
359.92	2650		0.33	Ottawa sand	[22]
6.82	2650	0.0036	0.679	sand, estimate	[22]

To quantify how much extrapolation would be needed to predict full-scale results using these lab-scale results, estimates of full-scale system parameters are required. Estimates of full-scale sediment and rotor wake characteristics are given in previous studies, and are shown in table 3.2. From this table, values of the five similarity parameters proposed by Glucksman-Glaser [19] and values of parameters $\mathbb{A}$ and $\mathbb{B}$ from the current work can be estimated. Parameter $\mathbb{C}$ can not be estimated without an estimate of the turbulent kinetic energy in a full-scale rotor wake.

Figure 3.43 shows the lab-scale and estimated full-scale values of Glucksman-Glaser's five vortex-based similarity parameters. The lab-scale values are lower than the full-scale values in almost all cases. Since the circulation or peak swirl velocity are in the numerator of each of these scaling parameters and the threshold friction velocity and/or terminal velocity are in the denominator of each parameter, the trend of lab scale below full scale indicates that the relative values of the vortex magnitudes to the sediment characteristics are lower in the lab-scale cases than in the full-scale cases. To match the lab scale to full scale, stronger vortices (caused by a higher blade loading, possibly) or more easily mobilized sediment would be necessary.

Figure 3.44 shows the lab-scale and full-scale values of the parameter groups identified in this work. The full scale values are primarily lower than the lab scale for parameter $\mathbb{A}$ and primarily higher than the lab-scale values for parameter $\mathbb{B}$. These trends conflict with those of Glucksman-Glaser's similarity parameters. If these results are considered without accounting for rotor radius or fluid density, the observed trends indicate instead that the lab scale ought to have weaker vortices or less easily mobilized sediment. Additionally, the full-scale sediment uplift predicted by parameters $\mathbb{A}$ and $\mathbb{B}$ conflict with each other. The lower half of estimates using parameter $\mathbb{A}$ predict no sediment mobilization at all and the maximum full-scale

value predicts an insignificant 3200 particles uplifted[3]. On the other hand, parameter $\mathbb{B}$ estimates between 10^{12} and 10^{19} particles uplifted. This prediction is clearly unreasonable; by some estimates 10^{19} is more sand grains than exist on Earth.

The disparity and impossibility of these predictions reinforce the hypothesis that the untested dependencies (primarily rotor radius and fluid density) have a significant effect on sediment mobilization. This is not surprising, but it is still useful to see supporting evidence. It is clear at this point that the dependencies identified in this work either require additional parameters to extend to full-scale predictions.

A useful extension of this work would be to test the system dependency on rotor radius and fluid density by applying the procedures in this work to experiments at different scales and in different fluids (testing in air or glycerin, for example). Additionally, several of the coupled system characteristics could be uncoupled by testing rotors with different blade loading coefficients and different number of blades. Because this increases the parameter space by two to four dimensions, this would require a very large amount of data collection. However, the results of that work could allow for full-scale predictions based on lab-scale data and could help identify more complete (and potentially dimensionless) similarity parameters.

[3]Remember that this prediction corresponds only to a nominally two-dimensional section of the rotor wake. The total number of mobilized sediment particles would be much higher, but not so much higher that 3200 sand grains could be called brownout.

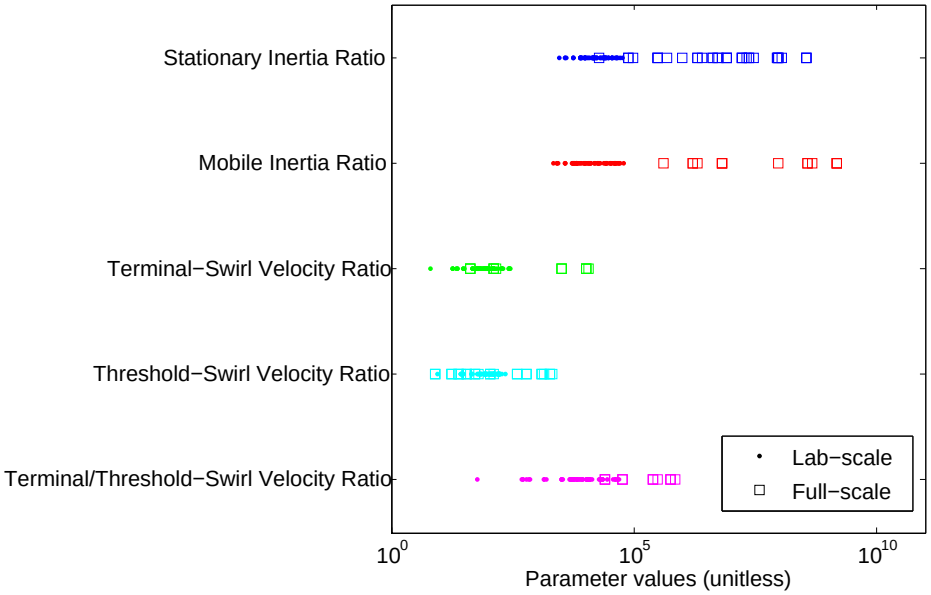

Figure 3.43: Full-scale estimates for Glucksman-Glaser's parameters [19]

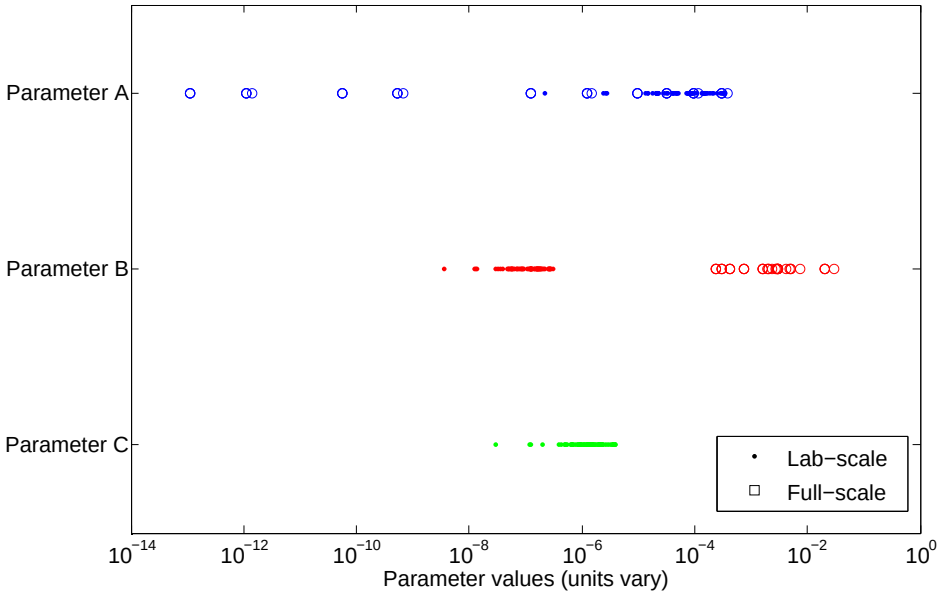

Figure 3.44: Full-scale estimates for proposed parameters

3.4.6 Field application

In a laboratory, measurements of each of the two-phase flow characteristics (such as vortex circulation or particle terminal velocity) can be made in order to determine the scaling parameter values. In the field, however, it is not possible to make precise measurements of the flow. Instead, it is necessary to estimate wake characteristics based on known system parameters. Of the three parameters proposed here, parameter $\mathbb{A}$ is the most easily estimated.

For any helicopter, several parameters are known. In particular, the crew will know the weight of the vehicle and the number and speed of the blades. For a hovering helicopter, the thrust from the rotor is roughly equal to the weight. From the total thrust and the rotor properties, the coefficient of thrust can be found from:

$$C_T = \frac{T}{\rho \pi \Omega^2 R^4}$$

From this, the bound circulation of the blade can be estimated. By conservation of circulation, the circulation of the tip vortex is equal to that of the blade, so that:

$$\Gamma_v = k \Omega R c \left(\frac{C_T}{\sigma} \right)$$

Here, k refers to the constant determined by the Kutta-Joukowski theorem. For an ideal rotor, $k = 2$, but empirically it has been determined that $k \approx 2.3$ [17]. The vortex peak swirl velocity is related to the vortex circulation by the vortex

core radius. The vortex core radius is not directly known, but it has been shown empirically that vortex core radius is roughly constant for full-sized helicopters. Substituting these values, parameter $\mathbb{A}$ can be estimated using:

$$\mathbb{A} = \frac{D_p^{2.5} V_{\theta\,\max}^2}{U_{*t}^3} \approx \frac{kW}{2\pi R_c N_b \rho \Omega R^2}(1 - e^{-\alpha})$$

Each of the parameters in this equation is known for any particular helicopter. This simplification allows the application of parameter $\mathbb{A}$ using only commonly known vehicle characteristics. However, the limitations described above still apply to the simplified version; the unknown dependencies of the system on rotor radius and fluid density must be addressed before this is put into practice.

3.5 Summary

In this chapter the results of the processing described in chapter 2 were shown. This began with an example PIV image frame and its associated velocity field. This velocity field was analyzed using the tracking Γ_1 function to locate blade tip vortices. The vortices were each fit with a Lamb-Oseen vortex model in order to quantify Γ_v, $V_{\theta\,\max}$, and R_c. Additionally, the velocity field was assessed in terms of turbulent kinetic energy and wall jet velocity. Trends in each of these versus rotor speed were discussed. Following this, the PIV image was filtered to isolate and quantify the dispersed phase. These sediment measurements were inspected for variance and frequency content. Both of these indicated that sediment uplift varies aperiodically. Trends in sediment uplift versus rotor speed were also presented. For each sediment

type, sediment uplift increases with increasing rotor speed. Significantly more sediment mobilization was experienced by the 98 µm glass particles than either of the others.

This chapter also investigated rotor-induced sediment mobilization system parameters for system dependencies. The results of Buckingham-Π dimensional analysis were tested and shown to correlate with sediment mobilization for each sediment type separately, but not for all sediment types together. Dimensioned parameters were then formed and inspected for correlation with all data and with data for each sediment type. Three of these parameters were identified and discussed. Dimensionless variations of these parameters were created and discussed. The dimensionless parameters did not display correlation with sediment mobilization. Extension of the proposed scaling parameters to full-scale rotor-induced sediment mobilization requires further study of the effects of varied fluid density and rotor radius.

Chapter 4: Conclusion

4.1 Summary

This thesis has described a procedure for the investigation of system dependencies in rotor-induced sediment mobilization. Carrier phase PIV and dispersed phase quantification of two-phase image data were used to compare the characteristics of rotor-induced flow to the resulting sediment mobilization. The processing of the dispersed sediment phase resulted in a mean number of sediment particles visible in a two-dimensional region of the rotor wake flow. The processing of the carrier fluid phase resulted in mean scalar quantities which characterized the rotor wake in terms of the blade tip vortices, the wall-jet velocity, and the turbulent kinetic energy. Characteristics of the sediment, rotor, and rotor wake were combined into many parameter groups and each group was inspected for correlation with the measured sediment mobilization. Three of these parameter groups were discussed more thoroughly.

The primary lessons learned in this thesis are:

1. PIV measurement of two-phase rotor-induced sediment mobilization can be separated into carrier phase velocities for wake characterization and dispersed phase locations for sediment uplift quantification. This method accurately measures each phase in cases of low dispersed phase concentration, but fails to do so when the suspended sediment becomes optically dense.

2. A rotor wake in ground effect can be more completely characterized by the identification and measurement of blade tip vortices. These vortices are visible in instantaneous PIV measurements and identifiable using the Γ_1 function.

3. For the field of view observed in this thesis, rotor tip vortices can be characterized by assigning to each a best-fit Lamb–Oseen vortex velocity profile. This method produces measurements of circulation (Γ_v), peak swirl velocity ($V_{\theta\,\max}$), and core radius (R_c) for each vortex.

4. Frequency analysis of identified sediment quantity over time does not show an amplitude peak at the vortex passage frequency. The primary frequency components are integer multiples of this frequency, suggesting that aperiodic events such as vortex bundling may be a primary cause of sediment uplift.

5. Time-averaged sediment uplift correlates with several parameter groups. In particular, parameter $\mathbb{A} = \frac{D_p^{2.5} V_{\theta\,\max}^2}{U_{*t}^3}$ has potential for use to predict sediment uplift based on particle and blade tip vortex characteristics.

4.2 Applications

Parameters $\mathbb{A}$, $\mathbb{B}$, and $\mathbb{C}$ can be used to predict the mean number of sediment particles visible in the field of view based on characteristics of the sediment, rotor, and wake. This prediction is only necessarily accurate within the limits of the parameter space tested here, and for rotor-induced sediment mobilization models which only vary the same 9 parameters inspected here (see table 3.1). This requires the use of water as the fluid phase and a rotor of the same radius (85 mm). Despite these restrictions, this allows measurements of wake properties to be used to predict sediment mobilization for cases which do not experimentally contain any sediment. These cases are simpler to test and can provide an easier means of estimating the effect of rotor modifications on the resulting rotor-induced sediment mobilization.

Parameter $\mathbb{A}$ requires measurement of sediment and tip vortex characteristics. Parameter $\mathbb{B}$ requires these and measurement of the wall-jet velocity. Parameter $\mathbb{C}$ additionally requires measurement of turbulent kinetic energy. Because the additional measurement of turbulent kinetic energy does not add significant accuracy to parameter $\mathbb{C}$, it is advisable to use parameter $\mathbb{A}$ or $\mathbb{B}$ for rotor-induced sediment mobilization comparison and prediction.

4.3 Limitations

The procedure described in this thesis has several limitations which are inherent to the techniques used in data recording and processing.

4.3.1 Field of view

As mentioned previously, the results of this procedure are sensitive to the field of view in which the experimental data is recorded. For all cases inspected here, the field of view was identical. It would be difficult, however, to duplicate this data closely using another system unless the same field of view could be captured. It is expected that the trends observed would be the same for data recorded using a different field of view, even though the numerical values of each data point would not be the same. Because of this limitation, the procedure described in this thesis cannot easily be used to retroactively compare existing data from separate facilities under varying conditions and scales. With proper planning, this procedure could be applied to future experiments if they are designed to have the same rotor-normalized field of view.

4.3.2 Optical density

This procedure is a variation of two-phase PIV, an optical measurement technique. There are significant advantages to optical techniques, such as the ability to simultaneously measure a large region of an experiment in high resolution. However, there are obvious drawbacks to the use of an optical measurement technique to study a phenomenon for which the primary characteristic of interest is the hazard caused by its opacity. Rotor-induced sediment mobilization in full force is not well suited to measurement using PIV. This was seen even in this lab-scale experiment; some of the data was removed due to the processing errors caused by increased optical

density. This places a limitation on this procedure to only be used in situations for which the resulting rotor-induced sediment mobilization is not too severe. This creates restrictions on the available parameter space, and may make it difficult to further test the proposed parameter groups.

4.3.3 Dimensionless parameters

In the creation of scaling parameters, it is desirable to normalize each in such a way that leaves the parameter dimensionless. Any field of study will have its own customary normalization scales, such as airfoil chord or rotor radius in the field of aerodynamics. However, the parameter groups proposed here were designed to incorporate all flow characteristics, leaving no independent scale with which to normalize. Because of this, the normalization of these parameters disrupted their correlation with sediment mobilization. Correlation of sediment mobilization to system characteristics was found for dimensioned parameter groups, but that correlation was not able to be maintained after normalization.

4.3.4 Extrapolation

This thesis has identified trends of sediment uplift with respect to groups of rotor wake and sediment characteristics. Within the range spanned for each parameter proposed here, the expected sediment uplift can be calculated based on measurements of the flow conditions. However, extrapolation beyond these limits would be required to predict the sediment uplift of a full scale helicopter. This

extrapolation would extend the predicted sediment uplift beyond the limits of optical measurement (as discussed above). Additionally, extrapolation may extend into flow regimes with high enough sediment density to experience two-way and four-way coupling of momentum transfer.[1] This coupling would change the correlation in ways which can not be seen in the flow regime measured for this thesis.

4.4 Further Research

Additional experimentation could begin to address these limitations. Suggestions for further research are given below.

4.4.1 Expanded parameter space

The application of this procedure to data collected for different model rotors, different sediments, and different fluids would expand the measured parameter space. This would more thoroughly test the proposed parameters, and would provide the required data to test modified or new scaling parameters as needed. Additionally, the use of rotors of varied chord, blade number, and pitch could decouple flow characteristics such as rotor speed and vortex circulation, which in this thesis could not be changed independently.

[1] For low sediment concentrations, it is assumed that the only transfer of momentum is from the fluid to the sediment. This is one-way transfer. Two-way coupling occurs for higher concentrations, where there can be significant momentum transfer from the sediment back to the fluid. Four-way coupling adds to these the momentum transfer from one particle to a second (and inherently the second particle to the first) in a collision.

The 81 cases investigated in this thesis varied 9 system parameters (table 3.1). However, the rotor radius and the fluid density remained the same in all cases. Measurements of flow conditions which vary in rotor radius and fluid density could identify correlations between these characteristics and the resulting sediment mobilization. Adapting the proposed parameters to address the correlations revealed by this additional data would enable their use in predicting full-scale rotor-induced sediment mobilization.

The parameter space could be extended using the same hardware described in this thesis. Leaving out the water (and thus using air as the fluid phase) would show the effects of fluid density on sediment mobilization. Replacing the rotor with one of a different pitch or chord would begin to decouple characteristics of the rotor and rotor-induced flow. The tank places constraints of scale, but a slightly larger rotor (perhaps 1.5 times the radius) could be operated in both water and air to further investigate scaling effects.

4.4.2 Field of view

The procedure described in this thesis quantifies sediment uplift and wake characteristics in a manner which is specific to the field of view. Because of this, only data acquired for this work was able to be used in the analysis of rotor-induced sediment mobilization system dependencies. If a wake characterization method that is independent of field of view was available, the analysis could have been much more thorough. The development of such a method would be a significant contribution

to studies of rotor-induced sediment mobilization. If such a method cannot be practically developed, future work could propose a standardized field of view for PIV measurement of rotor-induced sediment mobilization.

Bibliography

[1] Mapes, P., Kent, R., and Wood, R., "DoD Helicopter Mishaps FY85-05: Findings and Recommendations," Tech. rep., U.S. Air Force, 2008.

[2] Thomas, W., Hong, S. C., Yu, C. J., and Rosenzweig, E. L., "Enhanced Erosion Protection for Rotor Blades," *Proceedings of the 65th Annual Forum of the American Helicopter Society*, Grapevine, TX, May 27–29, 2009.

[3] Milluzzo, J., and Leishman, J. G., "Assessment of Rotorcraft Brownout Severity in Terms of Rotor Design Parameters," *Journal of the American Helicopter Society*, Vol. 55, No. 3, DOI: 10.4050/JAHS.55.032000, October 2010.

[4] White, R. P., Jr. and Vidal, R. J., "Study of the VTOL Downwash Impingement Problem," Tech. rep., U.S. Army and Cornell University, 1960.

[5] Kuhn, R. E., "An investigation to determine conditions under which downwash from VTOL aircraft will start surface erosion from various types of terrain," Tech. rep., NASA, 1959.

[6] Nathan, N. and Green, R., "Measurements of a Rotor Flow in Ground Effect and Visualization of the Brown-Out Phenomenon," *Proceedings of the 64th Annual Forum of the American Helicopter Society International*, April 29–May 1, 2008.

[7] Johnson, B., Leishman, J. G., and Sydney, A., "Investigation of Sediment Entrainment in Brownout Using High-Speed Particle Image Velocimetry," *65th Annual National Forum of the American Helicopter Society*, Grapevine, TX, May 27–29 2009.

[8] Bagnold, R. A., *The Physics of Blown Sand and Desert Dunes*, Dover Publications, Inc., Mineola, NY, 1941.

[9] Knight, M., and Hefner, R. A., "Analysis of Ground Effect on the Lifting Airscrew," National Advisory Committee for Aeronautics (NACA) Technical Note 835, 1941.

[10] Hayden, J. S., "The Effect of the Ground on Helicopter Hovering Power Required," *Proceedings of the 32nd Annual National V/STOL Forum of the American Helicopter Society*, Washington D.C., May 10–12, 1976.

[11] Curtiss, H. C., Sun, M., Putman, W. F., and Hanker, E. J., "Rotor Aerodynamics in Ground Effect at Low Advance Ratios," *Journal of the American Helicopter Society*, Vol. 29, No. 1, 1984, pp. 48–55.

[12] Milluzzo, J., Sydney, A., Rauleder, J., and Leishman, J. G., "In-Ground-Effect Aerodynamics of Rotors with Different Blade Tips," *Proceedings of the 66th Annual Forum of the American Helicopter Society*, Phoenix, AZ, May 10-13, 2010.

[13] Sydney, A., Baharani, A., and Leishman, J. G., "Understanding Brownout using Near-Wall Dual-Phase Flow Measurements," *Proceedings of the 67th Annual Forum of the American Helicopter Society*, Virginia Beach, VA, May 3-5, 2011.

[14] Lee, T. E., Leishman, J. G., and Ramasamy, M., "Fluid Dynamics of Interacting Blade Tip Vortices With a Ground Plane," *Journal of the American Helicopter Society*, Vol. 55, No. 2, April 2010, pp. 1–16.

[15] Light, J. S., and Norman, T., "Tip Vortex Geometry of a Hovering Helicopter Rotor in Ground Effect," *Proceedings of the 45th Annual Forum of the American Helicopter Society*, Boston, MA, May 22–24, 1989.

[16] Glucksman-Glaser, M. S. and Jones, A. R., "Effects of Model Scaling on Sediment Transport in Brownout," *AIAA Applied Aerodynamics Conference*, 2012.

[17] Leishman, J. G., *Principles of Helicopter Aerodynamics*, Cambridge University Press, New York, NY, 2nd ed., 2006.

[18] Greeley, R., and Iversen, J. D., *Wind as a Geological Process*, Cambridge University Press, New York, NY, 1985.

[19] Glucksman-Glaser, M. S., *The Effects of Model Scaling on Sediment Transport in Brownout*, Master's thesis, University of Maryland, College Park, 2013.

[20] Shao, Y. and Lu, H., "A Simple Expression for Wind Erosion Threshold Friction Velocity," *Journal of Geophysical Research*, Vol. 105, No. D17, 2000, pp. 22.

[21] "Sandblaster 2 Support of See-Through Technologies for Particulate Brownout," Tech. Rep., Task 5 Final Technical Report, Sponsored by Defense Advanced Research Projects Agency (DOD) Strategic Technology Office, Issued by U.S. Army Aviation and Missile Command under Contract No. W31P4Q-07-C-0215, MRI Project No. 110565, October 31, 2007.

[22] Baharani, A. K., *Investigation into the Effects of Aeolian Scaling Parameters on Sediment Mobilization Below a Hovering Rotor*, M.Sc. Thesis, University of Maryland, College Park, 2011.

[23] Adrian, R. J. and Westerweel, J., *Particle Image Velocimetry*, Cambridge University Press, New York, NY, 2010.

[24] Sydney, A. J., *Contributions Towards the Understanding of Rotor-Induced Dust Particle Mobilization and Transport*, Ph.D. thesis, University of Maryland, 2014.

[25] Kiger, K. T. and Pan, C., "PIV Technique for the Simultaneous Measurement of Dilute Two-Phase Flows," *Journal of Fluids Engineering*, Vol. 122, 2000, pp. 811–818.

[26] Mulinti, R. and Kiger, K. T., "Particle Suspension by a Forced Jet Impinging on a mobile Sediment Bed," *16th Int Symp on Applications of Laser Techniques to Fluid Mechanics*, 2012.

[27] Khalitov, D. A. and Longmire, E. K., "Simultaneous two-phase PIV by two-parameter phase discrimination," *Experiments in Fluids*, Vol. 32, 2002, pp. 252–268.

[28] Knowles, P. L. and Kiger, K. T., "Quantification of dispersed phase concentration using light sheet imaging methods," *Exp Fluids*, 2011.

[29] Graftieaux, L. and Michard, M. and Grosjean, N., "Combining PIV, POD and Vortex Identification Algorithms for the Study of Unsteady Turbulent Swirling Flows," *Measurement Science and Technology*, Vol. 12, No. 9, 2001, pp. 1422.

[30] Cotel, A. J. and Breidenthal, R. E., "Turbulence Inside a Vortex," *Physics of Fluids*, Vol. 11, 1999, pp. 3026–3029.

[31] Schlichting, *Boundary-Layer Theory*, McGraw-Hill, 1968.

[32] Leese, G.W., and Knight, J.T., Jr., "Helicopter Downwash Data," U.S. Army Engineer Waterways Experiment Station, Soils and Pavement Laboratory, Vicksburg, MS, June 1974.

[33] Boatwright, D. W., "Measurements of Velocity Components in the Wake of a Full-Scale Helicopter Rotor in Hover," Tech. rep., Mississippi State University, 1972.

[34] Ryerson, C. C., Haehnel, R. B., and Koenig, G. G., "Visibility Enhancement in Rotorwash Clouds," *43rd AIAA Aerospace Sciences Meeting and Exhibit*, 2005.